This is a repository copy of *Signatures of komatiite reactive melt flow through the Archaean Kaapvaal cratonic mantle*.

Version: Accepted Version

Article:

Daczko, N.R., Kamber, B.S., Gardner, R.L. et al. (2 more authors) (2024) Signatures of komatiite reactive melt flow through the Archaean Kaapvaal cratonic mantle. Contributions to Mineralogy and Petrology, 180. 5. ISSN 0010-7999

https://doi.org/10.1007/s00410-024-02188-z

Signatures of Komatiite Reactive Melt Flow through the Archaean Kaapvaal Cratonic Mantle

Submitted to *Contribution to Mineralogy and Petrology*

N. R. Daczko[a*], B. S. Kamber[b], R. L. Gardner[a], S. Piazolo[c], and H.E. Cathey[b]

[a]School of Natural Sciences, Macquarie University, Sydney, NSW 2109, Australia

[b]School of Earth and Atmospheric Sciences, Queensland University of Technology, Brisbane, QLD 4001, Australia

[c]School of Earth and Environment, University of Leeds, Leeds LS2 9JT, United Kingdom

*corresponding author: nathan.daczko@mq.edu.au

Abstract

Abundant Archaean komatiite and basalt erupted through evolving cratons, indicating melt transfer through the ancient mantle lithosphere. However, this process has rarely been identified in cratonic peridotite xenoliths, in contrast to exposed Phanerozoic mantle sections where melt-rock reactions are well-documented. We present a combined microstructural and mineral chemical investigation of eight coarse-grained (up to 20 mm), silica-rich, spinel facies peridotites from the Kaapvaal craton. These peridotites exhibit mild to strong silica-excess with 30–55 vol.% orthopyroxene. Microstructural evidence of former melt presence is abundant in all samples, including low apparent dihedral angles, irregular grain boundaries, and extremely elongate grains. Despite varying silica-excess, all peridotites are highly refractory, with olivine Fo-content of 92.9±0.3, reconstituted whole rock Mg-number of 92.9 ±0.4, and negligible TiO_2 concentrations. Thermobarometry and comparisons with experimental compositions and thermodynamic models suggest a continuum of reactions in open systems, where evolving komatiite melt sourced from greater depth interacted with precursor mantle lithosphere at 2–3 GPa. We propose that silica-excess in cratonic spinel peridotites results from high time-integrated (i.e., aggregated) melt flux through melt channels, without requiring a highly silicic melt. Evidence for reactive flow of komatiite melt through cratonic mantle supports an intraplate setting for many Archaean greenstone belts and a co-evolution of Archaean crust and mantle.

Keywords: cratonic peridotite; melt-rock interaction; high-energy grain boundaries; symplectite; excess silica; komatiite

Introduction

The subcontinental lithospheric mantle within Archaean cratons, referred to as the 'cratonic mantle', is one of Earth's oldest geochemical reservoirs. It differs from post-Archaean mantle lithosphere in being more melt-depleted (termed refractory), generally thicker (200–250 vs. <150 km), variably silica-enriched and occasionally diamondiferous (e.g., Pearson et al., 2021). Rhenium-Osmium dating of peridotitic sulphides and sulphide diamond-inclusions has yielded Re-depletion model ages suggestive of a protracted history of melt-extraction (e.g., Pearson et al., 1995). Notably, for the cratons formed over more than 500 Myr (e.g., Siberia, Kaapvaal, Zimbabwe, and Slave cratons), the sulphide Re-depletion ages often coincide with major igneous events shaping the overlying crust (e.g., Aulbach et al., 2004; Pearson et al., 1999; Simon et al., 2007; Smith et al., 2009).

This enduring magmatic activity requires the ascent of vast volumes of Neoarchaean mafic and ultramafic magmas (e.g., Condie, 1998) through mechanically strong cratonic mantle that had started forming 500–1000 Myr earlier. However, the mechanisms and locations of the implied melt migration and the relationship between komatiite and basalt melts remains largely speculative. Petrological, geochemical, and structural investigations of cratonic peridotites have uncovered a vertical stratification within the mantle root. Deeper samples, including those from the interpreted lithosphere-asthenosphere boundary (LAB), exhibit heightened deformation, variable chemical refertilisation (e.g., Griffin et al., 2003), and equilibration at temperatures surpassing the steady-state conductive geotherm (e.g., Boyd & Nixon, 1973). These features are commonly attributed to post-Archaean deformation, thermal perturbation and interactions with magmas and fluids from deeper sources (e.g., Gibson et al., 2013).

Specifically, in the Kaapvaal craton, Baptiste et al. (2012) documented a prevalence of sheared peridotites at depths exceeding 140 km, contrasting with shallower samples dominated by less deformed, mostly coarse-grained harzburgites. A similar depth-dependant distribution exists in the Siberian cratonic mantle (Bascou et al., 2011). Seismic studies qualitatively support these petrological models, revealing an anisotropic shallower layer (<~125 km; e.g., Sodoudi et al., 2013) overlying a deeper isotropic layer (~125–140 km), often separated by mid-lithospheric discontinuities (e.g., Boyce et al., 2024). The interpretations of seismic data can be supported by xenolith studies that determine the strength of the mineral crystallographic preferred orientation (CPO) using Electron Backscatter Diffraction (EBSD) data (e.g. Bascou et al., 2011).

There are only scarce petrological investigations into the shallower (60–120 km deep) cratonic peridotites, with few reporting evidence of melt-rock interaction that is expected from the long-lived mafic-ultramafic magmatic record in the overlying crust. At this depth range, spinel-, spinel+garnet- and garnet-facies harzburgites and clinopyroxene-poor lherzolites dominate (Fig. 1a; Griffin et al., 2003). Many of these peridotites belong to the ‘coarse granular’ and ‘tabular granular’ types of Boullier and Nicolas (1975), displaying little internal crystal deformation, and interesting curved (i.e., high energy) olivine-orthopyroxene grain boundaries.

A long-debated feature of many coarse-grained cratonic mantle peridotites is the source of excess orthopyroxene (Fig. 1a, Opx > 30 vol.% with the spinel facies), coexisting with highly forsteritic olivine ($Fo_{92.5–93.5}$; grey band, Fig. 1b), beyond that measured for experimental melt residues (inverted yellow triangles, Fig. 1b; Walter, 1998). Among the Kaapvaal peridotite xenoliths, the spinel facies samples are particularly enriched in orthopyroxene (Fig. 1), while olivine-rich samples are more common in the garnet facies (Tomlinson & Kamber, 2021, their figure 2d). The utilisation of thermodynamic databases and activity-composition models (Tomlinson & Holland, 2021), as highlighted in the work by Tomlinson and Kamber (2021) and Walsh et al. (2023), has conclusively demonstrated the incapacity of melt extraction alone to generate orthopyroxene-rich harzburgite residues, matching the experiments of Walter (1998). While basalt is common in the Archaean crust, its infiltration and reaction with preexisting peridotite lithosphere forms ‘fertilised’ lherzolite with less magnesian olivine (Le Roux et al., 2007) compared to the cratonic peridotites with excess orthopyroxene. This precludes a role for basalt in the formation of these high-silica peridotites and focuses attention on the potential role of interaction of peridotites with komatiite melt.

Additional hybridisation (infiltration and reaction) models made by Tomlinson and Kamber (2021) and Walsh et al. (2023) affirm that interaction between komatiite (melt) and peridotite lithosphere (solid) can produce harzburgite residues that replicate some of the observed mineral modes and chemistries of cratonic mantle (Fig. 1c; inverted orange triangles; Tomlinson & Kamber, 2021; purple squares Walsh et al., 2023). While these researchers suggest that melt-rock interaction is key to forming silica-rich harzburgite (Fig. 1b), their infiltration and reaction models do not replicate the most silica-rich end-members (orthopyroxene up to 55 vol.%) of the cratonic mantle (Fig. 1c).

In this study, we use a multi-disciplinary approach, combining microstructures, mineral chemistry and modelling to investigate the most silica-rich end-member harzburgite xenoliths of the Kaapvaal craton (green symbols, Fig. 1). These are very coarse-grained, spinel facies, clinopyroxene-poor peridotites devoid of visible garnet. They offer a higher likelihood of preserving vestiges of original 'igneous' processes (Mercier & Nicolas, 1975). We document the dominant slip systems of olivine and orthopyroxene but cannot determine a CPO as each thin section has too few grains for a statistically valid analysis. We determine mineral modes and reconstituted bulk rock chemistry to provide data for comparison with infiltration and reaction modelling outputs (Tomlinson & Kamber, 2021; Walsh et al., 2023) and to calculate pressure-temperature conditions of equilibration. Additionally, we characterise microstructures indicative of the former presence of melt, including grains with high-energy 'curved' boundaries that terminate with low dihedral angles. We find a close match between reaction textures in the samples studied and predictions of the reaction sequence from the published thermodynamic infiltration and reaction models. We find that open-system, high-temperature, reactive flow of komatiite melt through peridotite progressively increases the mode of orthopyroxene in the melt-fluxed cratonic mantle, thus characterising the migration channels for vast volumes of Neoarchaean mafic and ultramafic magmas. This research contributes to the understanding of Archaean pathways of melt ascent through proto-cratonic mantle, providing insights into models of cratonic growth and evolution.

Samples and methods

Samples

We studied xenolith samples from the Bultfontein pans in the Kimberly cluster on the Kaapvaal craton, Republic of South Africa (28.739155°S, 24.818094°E). At this locality, many well-preserved coarse-grained peridotite xenoliths exist (Simon et al., 2007; Whitfield, 1973). Considering the aim of the study and the wide consensus that deeper (garnet-facies) peridotites likely experienced more extensive post-Archaean metasomatism and deformation, we focussed on garnet-free, visibly freshest, and least-deformed xenolith samples. These garnet-free ‘spinel-facies harzburgites’ can be divided into those with dominantly pale green-brown orthopyroxene and a group containing orthopyroxene of ‘bronzitic’ lustre (Fig. 2a, b respectively). Twelve samples were collected and examined with thin sections. The eight freshest were selected for this study.

We targeted the samples with coarse orthopyroxene of variably ‘bronzitic’ appearance (Fig. 2) as this optical effect, from light reflecting off crystallographically oriented clinopyroxene and spinel exsolution lamellae on cleavage planes (Fig. 2), is readily seen in the field. High proportions of lamellae indicate formerly Ca+Al+Cr-rich orthopyroxene (e.g., Mercier & Nicolas, 1975; Pike et al., 1977) which forms at high-temperatures, as shown by experimental data (e.g., Walter, 1998) and thermodynamic modelling results (Tomlinson & Kamber, 2021; Walsh et al., 2023). No peer-reviewed survey exists for the relative abundance of these coarse-grained ‘bronzitic’ spinel peridotites but based on the abundance of spinel-harzburgites s.l., our own observations, and the relative paucity of scientific research on them, we estimate these to make up 5–10% of the total peridotites at the Bultfontein pans. Although relatively rare, this type of peridotite xenolith is known from several kimberlites across the Kaapvaal craton (e.g., Baptiste et al., 2012), and many other cratons, including the Siberian (Bascou et al., 2011) and the Slave (Kopylova & Caro, 2004).

Methods

Detailed analytical conditions and methods used in this study are reported in Online Resource 1 (Supplementary Methods). Optical and electron microscopy used polarising (Olympus VS200) and scanning electron microscopes at both Macquarie University (Teneo Field Emission Gun Scanning Electron Microscope (FEG-SEM)) and Queensland University of Technology (Tescan MIRA3 FEG-SEM) to collect ultra-high-resolution photomicrographs and back-scattered electron (BSE) images. EBSD analysis was conducted at Leeds Electron Microscopy and Spectroscopy Centre, University of Leeds on a FEI Quanta 650 FEG- Environmental SEM equipped with a Symmetry EBSD detector (Oxford Instruments). Electron microprobe (EMP) analysis used a JEOL JXA 8530F FEG microprobe at Queensland University of Technology. When using mineral abbreviations, we follow the convention of Whitney and Evans (2010).

We used the published peridotite and hybrid peridotite-komatiite thermodynamic model outputs from Tomlinson and Kamber (2021) and Walsh et al. (2023) to calculate new stoichiometric assimilation-fractional-crystallisation (AFC) reactions. The AFC reactions were obtained by mass balance, comparing assemblages between the solidus peridotite and the hybrid peridotite-komatiite systems. Following the approach of Emo and Kamber (2022), the residual assemblage after melt escape can be investigated at any temperature in the hybrid peridotite-komatiite systems of Tomlinson and Kamber (2021) and Walsh et al. (2023). This allows a first-order assessment of open-system behaviour when modelled melts are removed from solid residues.

Additionally two new pressure-temperature pseudosections for deep (7 GPa) komatiite and a komatiite-harzburgite hybrid were calculated with MAGEMin in the NCKFMASHTOCr system using the THERMOCALC database (tc350) and the IGNEOUS SET (in MAGEMin) of phases and activity-composition models (Riel et al., 2022).

Results

Based on modal analysis (Table 1), the eight studied samples classify as five spinel harzburgites (Group 1) and three spinel lherzolites (Group 2), and of the latter, two contain trace quantities of garnet (Table 1). The clinopyroxene modal abundance of the Group 2 lherzolites (classified with the Le Bas and Streckeisen (1991) scheme) is at the lower limit for lherzolites, ranging from 5.4–7.6 vol.%. Compared to a global compilation of coarse grained, garnet-free cratonic peridotites, the studied samples fall in the orthopyroxene-rich range (Fig. 1a), with modal abundance ranging from 30–55 vol.%.

Detailed microstructure of representative samples

We analysed the fabric of six samples using combined optical microscopy, SEM BSE and EBSD data (excluding samples 17BSK040 and 043). Across the harzburgites and lherzolites, we found consistently developed microstructures and therefore only one of each is illustrated in detail with a representative specimen. The description begins with the fabric of the dominant rock forming minerals before analysing the details of finer-grained and more complex features.

Group 1 – Harzburgites

Harzburgite samples 17BSK041, 043, 045, 046 and 048 have a very simple primary mineral assemblage dominated entirely by olivine (Ol_1) and orthopyroxene (Opx_1) with minor clinopyroxene films (Cpx_1; Fig 2a inset), symplectites (Fig. 2b) of clinopyroxene (Cpx_2, up to 2.6 vol.%) and vermicular spinel (Spl_1; <1 vol.%), predominantly at olivine-orthopyroxene grain boundaries. Lamellae of clinopyroxene (Cpx_{lam}) and spinel (Spl_{lam}) are common in orthopyroxene (Opx_1; Fig. 2b upper inset) and lamellae of orthopyroxene (Opx_{lam}) and spinel (Spl_{lam}) are common in clinopyroxene (both Cpx_1 and Cpx_2; Fig. 2b lower inset). Olivine and orthopyroxene grain size is very coarse (up to > 20 mm long). Elongate orthopyroxene defines a weak shape preferred orientation (SPO) and foliation. Olivine and orthopyroxene grains have average aspect ratios of ~2 and maximum ratios of ~6 (Fig. 3). Grain shapes are highly irregular with smoothly curved boundaries of variable wavelength from undulating to tightly curved (Fig. 3). The latter may form apparent inclusions where the boundaries intersect the thin section from the third dimension. Some coarse grains of olivine and orthopyroxene have cuspate fingers that protrude along adjacent grain boundaries, while finer grains can form elongate mineral films. These may terminate with apparent low dihedral angles (Fig. 3b, d) or with curved tips (Fig. 3c). Rare 120° triple junctions are restricted to three like minerals intersections (Fig. 3d: Ol-Ol-Ol and 3f: Opx-Opx-Opx).

Within a neighbourhood of coarse grains, two or three apparently isolated grains can show the same extinction angle (Fig. 3f) and crystal orientation (Fig. 3a, b; see also pole figure insets). Olivine grains show undulose extinction, rarely with internal misorientation up to ~20° (Fig. 3b, inset, and Online Resource 2 – Supplementary Figure 1). In contrast, orthopyroxene grains show less internal misorientation, in places reaching up to ~10° (Fig. 3c, inset, and Online Resource 2 – Supplementary Figure 1).

Based on a small number (41–79) of coarse olivine grains (>500 µm) in each samples' thin section, the a, b and c axis pole figures (Online Resource 2 – Supplementary Figure 2) show transitional patterns between point clusters and girdles, inhibiting interpretation of a crystallographic preferred orientation (CPO). The dominant slip system analysis (Fig. 4) shows that the rotation axis for the olivine subgrain boundaries is predominantly around the olivine a-axis [100] (samples 17BSK046 and 048) and b-axis [010] (samples 17BSK041 and 045) (Fig. 4), with a dominant slip direction along the c-axis [001] in the a (100) or b (010) planes (i.e., the planes perpendicular to the a and b axes). This corresponds to type B and C slip systems of olivine (as recently summarised by Griffin et al., 2022).

Similarly, for the small number (31–63) of coarse orthopyroxene grains (>500 µm) in each thin section, the pole figures show near random patterns (Online Resource 2 – Supplementary Figure 2). The dominant slip system analysis shows that the rotation axis for the orthopyroxene subgrain boundaries is predominantly around the b-axis [010] (samples 17BSK046 and 048) or a combination of the c [001] and b [010] axes (samples 17BSK041 and 045) (Fig. 4). The dominant slip direction of orthopyroxene is consistently along the a-axis [100] in the b (010) or c (001) planes. This corresponds to type CA or BA slip systems of orthopyroxene ((as recently described by Bernard et al., 2021).

While films of clinopyroxene (Cpx_1; Fig 2a inset) are rare in group 1 harzburgites, clinopyroxene intergrown with spinel in symplectites (Fig. 2b) is common. These have a single orientation for each mineral within the intergrowth (Fig. 5). Clinopyroxene shows the same orientation on a- {100} and b- {010} axes as the adjacent orthopyroxene (Fig. 5, red and black dashed circles). Spinel {111} shows the same orientation as the pyroxenes {100} (Fig. 5c, red dashed circles), and spinel {110} has the same orientation as pyroxenes {010} (Fig. 5c, black dashed circles).

Group 2 – Lherzolites

Samples 17BSK039 (Fig. 6), 040 and 044 contain sufficient clinopyroxene (~5–8 vol.%) to classify as lherzolites (Fig. 1a). Olivine (Ol_1; Fig. 6b) and orthopyroxene (Opx_1; Fig. 6c) grain sizes, grain shapes, aspect ratios, and SPO are similar to the harzburgite samples. Clinopyroxene films (Cpx_1) form at olivine-orthopyroxene grain boundaries (Fig. 6a) and are more common than in the harzburgite samples. All samples also contain symplectites of clinopyroxene (Cpx_2) and vermicular spinel (Spl_1) like the first group of harzburgite samples (Fig. 5). Some clinopyroxene films (Cpx_1) and symplectites of clinopyroxene (Cpx_2) and vermicular spinel (Spl_1) in sample 17BSK039 (Fig. 6a) and 040 have thin garnet films (Grt_1) at the boundary with orthopyroxene. Other garnet films (Grt_1) occur along orthopyroxene grain boundaries (Fig. 6f) and in trails cutting orthopyroxene (Fig. 6f).

Sample 17BSK039 has a texturally distinct symplectite in which clinopyroxene (Cpx_3) is intergrown with garnet (Grt_2; ~1 vol.%), olivine (Ol_2) and spinel (Spl_2; ~0.6 vol.%) (Fig. 7a–c), hereafter referred to as the garnet-bearing symplectite. Two types of olivine occur within the large symplectite, distinguished by highly rounded (Ol_1; Fig. 7b, c, marked A) versus straight grain boundaries (Ol_2; Fig. 7d). Fine-grained amphibole (Fig. 7a) is predominantly observed in sample 17BSK039 and occurs at clinopyroxene–olivine grain boundaries.

Neighbourhoods of isolated coarse grains in lherzolite samples can show the same extinction angle and crystal orientation (grains labelled 1–4, Fig. 6b, c) similar to those seen in the harzburgite samples. Additionally, a neighbourhood of small, rounded olivine grains in sample 17BSK039 is observed within the garnet-bearing symplectite that have the same orientation (Fig. 7a–c, e marked A). The nearby fine olivine grains with straight boundaries have different orientations (Fig. 7d, grain labelled Ol_2) to the surrounding neighbourhood of rounded olivine grains. The crystallographic axes of adjacent coarse olivine grain B (Fig 7a–c) show no relationship to the orientations of any mineral within the symplectite.

Coarse grained orthopyroxene C (Fig. 7a–c) has the same crystal orientation for the a-{100} and b- {010} axes as the adjacent clinopyroxene grains G and H (Fig. 7a–c; Fig. 7e, green and black dashed lines). These clinopyroxene grains outside the symplectite have the same orientation as nearby grains within the symplectite. For example, three grains within the symplectite have the same orientation as the clinopyroxene grain H (Fig. 7c white arrows; see also grain G and similar coloured clinopyroxene within the symplectite). The crystallographic axes of coarse orthopyroxene grain D (Fig 7a–c) have the same orientation for the a- {100} and b- {010} axes (Online Resource 2 – Supplementary Figure 3b, yellow arrow c, green dashed line) as only one clinopyroxene grain (Online Resource 2 – Supplementary Figure 3b, yellow arrow) within the symplectite. The crystallographic axes of the other nearby coarse orthopyroxene grains E and F (Fig. 7) show no relationship to the orientations of any other nearby minerals. However, clinopyroxene lamellae within orthopyroxene grain E have the same orientation for the a- {100} and b- {010} axes (Online Resource 2 – Supplementary Figure 3c, black dashed lines).

The crystallographic axes of the garnet grain forming a film between orthopyroxene (F) and clinopyroxene (G) shows no relationship to the adjacent pyroxenes (Online Resource 2 – Supplementary Figure 3c blue data on garnet pole figure). Garnet within the symplectite has a single orientation with minor, non-systematic scattering. One of the three {100}-axes (garnet is cubic) has the same orientation as the b-axis {010} of the pyroxene grains C and G/H (Fig. 7e, black dashed line). In addition, two of the 6 {110} axes of garnet have the same orientation as the c-axis {001} of orthopyroxene grain C (blue dashed line) and a-axis {100} of the pyroxene grains C and G/H (green dashed line).

One of the three {100}-axes of spinel (it is also cubic) has the same orientation as the b-axis {010} of the pyroxene grains C and G/H and garnet within the symplectite (Fig. 7e, black dashed line). Another of the spinel {100}-axes has the same orientation as the c-axis {001} of the orthopyroxene grain C and the {110} axis of garnet (Fig. 7e, blue dashed line). In addition, one of the six {110} axes and one of the four {111} axes of spinel have the same orientation as the b {010} axis and c {001} axis of olivine grain A (Fig. 7e, purple and red dashed lines).

For the small number (42–51) of coarse olivine grains (>500 μm) in the two lherzolite samples studied with EBSD, the a, b and c axis pole figures (Online Resource 2 – Supplementary Figure 2) show transitional patterns between point clusters and girdles, inhibiting clear interpretation of a CPO. The dominant slip system analysis (Fig. 4) shows that the rotation axis for the olivine subgrain boundaries in sample 17BSK044 is predominantly around the olivine b-axis [010] (similar to harzburgite samples 17BSK041 and 045) (Fig. 4) with a dominant slip direction along the c-axis [001] in the a (100) or b (010) planes (i.e., the planes perpendicular to the a and b axes). This corresponds to type B and C slip systems of olivine (Griffin et al., 2022). The dominant slip system analysis (fig. 4) shows that the rotation axis for the olivine subgrain boundaries in sample 17BSK039 is predominantly around the olivine c-axis [001], most similar to harzburgite sample 048 (Fig. 4), with a dominant slip direction along the a-axis [100]. This corresponds to type A and D slip systems of olivine (Griffin et al., 2022).

For the small number (22–29) of coarse orthopyroxene grains (>500 μm) in each sample, the pole figures show near random patterns (Online Resource 2 – Supplementary Figure 2). In contrast to the harzburgite samples, the dominant slip system analysis shows that the rotation axis for the orthopyroxene subgrain boundaries is predominantly around the c-axis [001] (Fig. 4). This is consistent with type AB or BA slip systems of orthopyroxene (Bernard et al., 2021).

Mineral chemistry and geobarometry

Electron microprobe mineral chemical data (n: olivine = 212; orthopyroxene = 153; clinopyroxene = 134; spinel = 88; garnet = 44; amphibole = 35) were obtained on seven of the eight samples and all individual analyses are reported in Online Resource 3, with summary data in Online Resource 4.

In a plot of olivine modal abundance versus olivine forsterite content (Fig. 1b), the studied samples overlap with published olivine-poor spinel-harzburgites and lherzolites. Olivine in the harzburgites studied is slightly more forsterite-rich (93.0±0.1) than in the lherzolites (92.6±0.3) and the global compilation (Fig. 1b).

Group 1 – Harzburgites

In all analysed harzburgite samples (17BSK043, 045, 046 and 048), olivine (Online Resource 3b & 4b) and orthopyroxene (Online Resource 3c & 4c) are chemically homogeneous, regardless of microstructural context and likely different origins. For both minerals, the analyses were averaged within groups: coarse grains, apparent mutual inclusions, and cuspate fingers. There is no statistically significant difference in olivine chemistry between the textural types (Online Resource 3b & 4b; average Fo per sample = 93.06±0.05; 92.99±0.06; 93.00±0.06; and 93.17±0.04) and within the coarse grains there is no detectable chemical gradient (the median reproducibility for the forsterite content was 0.06%). We note from the number of attempted analyses (Online Resource 3b & c) that there are many more apparent inclusions of olivine in orthopyroxene than vice versa. All olivine has near constant NiO and MnO (0.36–0.41 wt.% and 0.09–0.10 wt.%, respectively).

Trace Ca was detected (0.01–0.02 wt.%), whereas, Ti and Na are consistently below the detection limits of 80 and 15 ppm, respectively. This is also true for the texturally distinct fine olivine grains adjacent to clinopyroxene films (Cpx_1; Fig. 2a inset) in sample 17BSK045 (analyses #9 and #15–18; Online Resource 3b). They are as refractory as the large rock-forming olivine. In samples 17BSK046 and 048, trace Al_2O_3 and Cr_2O_3 were detected in olivine at 0.005–0.007 and 0.004–0.008 wt.%, respectively (Online Resource 3b & 4b). In the other two harzburgites, Al and Cr were below their detection limits of 12 and 18 ppm, respectively, including in the grains adjacent to clinopyroxene films (Cpx_1).

The harzburgite orthopyroxenes are also chemically homogeneous (Online Resource 3c & 4c; average Mg# per sample = 93.56±0.06; 93.50±0.01; 93.50±0.05; and 93.57±0.08), with no discernible differences between coarse grains, cuspate fingers and, where present, apparent inclusions in olivine (sample 17BSK048 only). The Al_2O_3 (2.32±0.10 to 2.87±0.07 wt.%), Cr_2O_3 (0.72±0.05 to 0.87±0.03 wt.%) and CaO (0.74±0.09 to 0.92±0.14 wt.%) concentrations are high and homogeneous in all samples. Despite evidence for sub-micron width lamellae (Fig. 8b, c), the homogeneity in these three elements is maintained because analyses were performed with a defocussed 3-micron beam. Concentrations of TiO_2 (below detection limit) and Na_2O (0.01–0.02 wt.%) are very low. The only orthopyroxene that differs slightly in chemistry is from a clinopyroxene-spinel symplectite in sample 17BSK045. In general, its composition is slightly less magnesian (Mg# 92.8±0.1 versus 93.5±0.05 in the coarse grains) richer in Ni, but poorer in Cr, Al and Ca.

As with the main rock forming minerals, clinopyroxene is chemically homogeneous in harzburgites (Online Resource 3d & 4d; Mg-numbers = 95.2±1.1 to 95.7±0.2). In sample

17BSK045, clinopyroxene films (Cpx_1) are slightly more aluminous (2.33 vs. 1.96 wt.%) and less chromian (1.10 vs. 1.28 wt.%) than clinopyroxene (Cpx_2) intergrown with spinel. Clinopyroxene has minor Na_2O (0.56±0.02 to 0.66±0.42 wt.%) with Ti below detection limit (180 ppm).

In the harzburgites, spinel (Spl_1) occurs exclusively in symplectites with clinopyroxene (Cpx_2) and 45/48 analysed grains are chromian spinels, with Cr- and Mg-numbers of 0.57±0.03 and 0.63±0.03, respectively (Online Resource 3e & 4e). The three remaining grains have higher Cr-numbers (0.75–0.96) and classify as chromite (after Ferracutti et al., 2015) which have higher Fe^{3+}/Fe^{2+} ratios than the chromian spinels and, in sample 17BSK045, are associated with minor secondary Ca-carbonate in the symplectite.

Group 2 – Lherzolites

Olivine and orthopyroxene are also very homogeneous in the analysed lherzolites (17BSK039, 040, 044). Olivine is, on average, slightly less forsteritic in the lherzolites than in the harzburgites (Table 2; Fo = 92.6±0.3) but equally low in trace elements (Ti, Al, Cr, and Na). Concentrations of the remaining three oxides (NiO, MnO and CaO) are within error of those found in the harzburgites. Olivine in 17BSK044 was also analysed for K, which was also below detection limit (120 ppm).

Orthopyroxene analyses in lherzolites show greater chemical variability (i.e., higher standard deviations) than in harzburgites, particularly for Al_2O_3, Cr_2O_3, CaO and Na_2O (Online Resource 3c & 4c). This is likely due to the presence of coarser lamellae (Fig. 8c) that were not homogeneously sampled with the 3-micron wide beam. Analyses deliberately overlapped on wide lamellae have compositional trends towards clinopyroxene and spinel (Fig. 8a; see also Acevedo Zamora & Kamber, 2023), with spinel dominant.

Clinopyroxenes ($Cpx_{1–3}$) are chemically homogeneous in lherzolites (Online Resource 3d & 4d), although clinopyroxene (Cpx_2) intergrown with spinel (Spl_1) is lower in Cr and Al concentration compared with the other clinopyroxene types. Chromium concentrations are lower in all clinopyroxene in lherzolite (0.44±0.08 to 0.91±0.19 wt.%) compared with those in harzburgite (1.10±0.02 to 1.61±0.63 wt.%). Clinopyroxene analyses in lherzolites show chemical variability, i.e., standard deviations that are 2–4 times higher than analytical reproducibility for Al_2O_3, Cr_2O_3, SiO_2, MgO and CaO (Online Resource 3d & 4d). This is likely due to the presence of coarser lamellae (Fig. 8d). Analyses deliberately overlapped on wide lamellae have compositional trends towards orthopyroxene and spinel (Fig. 8a), with spinel dominant. In sample 17BSK040, lamellae-free clinopyroxene (Cpx_3) is more homogeneous and has the lowest Al and Cr concentrations (Online Resource 3d & 4d).

Spinel grains in the lherzolites are predominantly chromian spinels (35/40 analyses, Online Resource 3e & 4e) with Cr- and Mg-numbers of 0.59±0.11 and 0.57±0.10, indistinguishable from those in the harzburgites (Online Resource 3e & 4e). The five other spinel analyses have lower Cr-numbers and higher Mg-numbers (Online Resource 3e). Garnet ($Grt_{1\&2}$) in samples 17BSK039 and 040 is pyrope-rich and homogeneous, with low Cr_2O_3 (1.02±0.17 to 1.41±0.30 wt.%).

For the two garnet-bearing samples (17BSK039 and 040), equilibration temperatures and pressures (*PT*) were calculated using PTEXL v.2 (Stachel, 2022). Seven coexisting garnet-orthopyroxene-clinopyroxene assemblages in 17BSK039 yielded equilibration *PT* of 626±43°C at 2.9±0.4 GPa using the single clinopyroxene geothermobarometer of Nimis and Taylor (2000). Combining the two-pyroxene thermometer of Taylor (1998) and the Cr-in-clinopyroxene barometer of Sudholz et al. (2021) yielded *PT* of 617±42°C at 2.4±0.3 GPa. The same geobarometers applied to three garnet-orthopyroxene-clinopyroxene assemblages in 17BSK040 yielded equilibration *PT* of 631±22°C at 2.6±0.2 GPa and 618±26°C at 2.4±0.15 GPa. Within uncertainty, these estimates agree and point to equilibration on the typical modern Kaapvaal craton equilibrium geotherm (e.g., Hoare et al., 2022). The mismatch between the modelled temperatures of komatiite-peridotite interactions (Fig. 9, > 1500°C) and these geothermobarometer results (~600–650°C) show that no vestige of Archaean mineral chemistry was found in the studied xenoliths. However, the pressure results (~2.5–3GPa) indicate the komatiite-peridotite interaction occurred deep within the Archaean lithosphere. Finally, all three lherzolites also contain accessory chemically homogeneous amphibole Online Resource 3g & 4g, which is pargasite with Mg# of 91.6±0.1 to 92.4±0.2, SiO_2 = 44.4–46.3 wt.%, TiO_2 below detection limit and Na_2O 3.0-4.3 wt.%.

Assimilation-Fractional-Crystallisation (AFC) reactions

Stoichiometric assimilation-fractional-crystallisation (AFC) reactions (Fig. 9a, b) were determined by mass balance, comparing phase modes relative to the modes in the original system state. That is, 1:1 lherzolite (solid):komatiite (melt) (Fig. 9a, Tomlinson & Kamber, 2021) and 2:1 harzburgite (solid):komatiite (melt) (Fig. 9b, Walsh et al., 2023).

Across all temperature ranges olivine is enriched relative to the original system state and the positive slope in temperature range 6 indicates minor consumption of olivine approaching the solidus. At temperatures above 1580°C in the 1:1 lherzolite to komatiite system at 2 GPa (temperature range 0, Fig. 9a), all orthopyroxene, clinopyroxene and spinel in the pre-existing lherzolite is assimilated into the komatiite melt. A dunite residue would form if all this melt is extracted at these high temperatures (temperatures > 1580°C). Between 1580°C and 1546°C orthopyroxene is partially assimilated into the komatiite melt, such that its mode is decreased relative to the modes in the original system state (temperature range 1, Fig. 9a). Below 1546°C, the mode of orthopyroxene exceeds that of the pre-existing lherzolite. The continued growth of peritectic orthopyroxene from 1546 –1430°C enriches the mode of orthopyroxene well above that of the precursor lherzolite (temperature range 2, Fig. 9a). Across this orthopyroxene enrichment interval, the composition of the melt changes from komatiite (MgO = 23.4 wt.%) to high-Mg basalt (MgO = 15 wt.%). An orthopyroxene enriched harzburgite forms if the melt is extracted in this temperature range. Some orthopyroxene is consumed at temperatures below 1430°C (i.e., a positive slope at temperatures below the red star, Fig. 9a) forming ample clinopyroxene and minor spinel (temperature ranges 3–6, Fig. 9a) by the solidus of the hybridised system.

At temperatures above 1623°C in the 2:1 harzburgite to komatiite system at 3 GPa (temperature ranges 1 and 2, Fig. 9b), the mode changes are similar to that of the 1:1 lherzolite to komatiite system. Across the orthopyroxene growth interval (temperature ranges 2, 7 and 8, Fig. 9b) the composition of the melt remains komatiitic but the MgO content reduces from 27.2 to 18.3 wt.%. Below 1623°C, garnet is partially assimilated into the komatiite melt, such that its mode is decreased relative to the modes in the original system state (temperature ranges 2 and 7, Fig. 9b). Below 1522°C, reactions consume orthopyroxene and produce clinopyroxene, minor olivine and garnet as well as a less magnesian melt (temperature ranges 9 and 10, Fig. 9b). As the system approaches the solidus, the melt changes to basalt and minor clinopyroxene is consumed (temperature range 10 in Fig. 9b).

Discussion

Microstructures indicative of the former presence of melt and reactions

Several studies have examined coarse-grained cratonic peridotites characterised by low modes of clinopyroxene, spinel and garnet. These investigations noted curved grain boundaries (e.g., Boullier & Nicolas, 1975), interpenetrating boundaries between orthopyroxene and olivine (Baptiste et al., 2012), and grain shapes ranging from interlobate to vermicular, primarily for orthopyroxene (Simon et al., 2007). The latter study noted that orthopyroxene exhibited “vermicular extensions, giving them a melt-like appearance” (Simon et al., 2007, p.596). Most previous petrological research on cratonic peridotites that has referred to melt-solid interaction, invoked it for the growth of interstitial minerals – such as clinopyroxene, spinel, amphibole and phlogopite (e.g., Kopylova & Caro, 2004). In contrast, this study shows that the microstructures of olivine and orthopyroxene in ‘bronzitic’ xenolith samples also result from melt-rock interaction.

We use ultra-high resolution EBSD maps, BSE images and optical microscopy with four reliable microstructural criteria that are indicative of the former presence of melt (e.g., Basch et al., 2019; Daczko & Piazolo, 2022; Vernon, 2011) to demonstrate that the cratonic peridotite samples analysed formed by melt-rock interaction.

(1) Minerals that subtend to low (<60°) apparent dihedral angles including olivine (Fig. 3f), orthopyroxene (Fig. 3d), and clinopyroxene (Fig. 6e) where the mineral forming the small dihedral angle is interpreted to have crystallised from melt at the junction of two solid grains.

(2) High energy grain boundaries indicated by highly irregular coarse grain shapes, with undulations, short cuspate extensions and tight curves (Figs. 3a and 6a). These high energy boundaries are ubiquitous for both olivine and orthopyroxene (Fig. 3a). This microstructure is like that formed by the impingement of minerals on each other during the final stages of crystallisation in igneous rocks (Vernon, 2018).

(3) EBSD crystal orientation data, and/or similar extinction angles identify neighbourhoods of apparently separate grains of olivine and orthopyroxene (Fig. 3b, c, f; Fig. 6b, c, e), which are likely a single grain connected in 3D (i.e., with branching grain shapes). These are inferred to represent crystallised grain boundary melt networks (Stuart et al., 2018).

(4) Extremely elongate minerals (aspect ratios ~10; Stuart et al., 2018) usually form fingers that extend from larger grains of olivine (Fig. 3f) or orthopyroxene (Fig. 3d, e) and represent crystallisation of melt at wetted grain boundaries. Additionally, thick clinopyroxene mineral films in lherzolite sample 17BSK039 (Fig. 6a, d, e) and rarely in harzburgite sample 17BSK045 (Fig. 2a insets) are inferred sites of melt crystallisation and melt-rock interaction, partially replacing adjacent olivine and/or orthopyroxene grains.

The analysis of the microstructures within the main rock forming minerals, namely olivine and orthopyroxene, confirms the important role of melt in transforming grain sizes, shapes and boundaries in all examined harzburgite and lherzolite samples. These microstructures, including the overall coarse grain size and the high energy grain boundaries, indicate significant modification of the peridotite and are ubiquitous throughout the samples. These high-energy microstructures have been preserved since the Archaean, likely due to the very coarse grain size, even though the mineral chemistry re-equilibrated to the cratonic geotherm. The key reaction inferred from the microstructures is the extensive melt-mediated replacement of former peridotite by the olivine (Ol_1) and orthopyroxene (Opx_1) minerals in the studied harzburgite and lherzolite samples (see reaction R1 below). The high concentrations of Al and Cr in the studied harzburgitic orthopyroxenes further imply that the reaction occurred at very high temperatures and in the absence of garnet and spinel. Orthopyroxene in garnet harzburgites has Al_2O_3 concentration lower than 0.8 wt.% (e.g., Simon et al., 2007; Wasch et al., 2009) whereas our coarse-grained harzburgitic orthopyroxenes have Al_2O_3 between 2.3 and 2.9 w.t%. Kaapvaal craton spinel-peridotite orthopyroxenes have Cr_2O_3 concentrations (0.22±0.10 wt.%; Simon et al., 2007) much lower than in our coarse-grained samples (0.83±0.06 wt.%).

Thin clinopyroxene (Cpx_1) films in harzburgite (Fig. 2a, inset) and thick films in lherzolite (Fig. 2b, 6) formed after some orthopyroxene as shown by the topotaxic relationship with adjacent orthopyroxene (Opx_1) (Fig. 7e; see reaction R2 below). This melt-rock interaction formed microstructures that are unusual compared with Phanerozoic mantle xenoliths, which normally show a finer-grained granoblastic microstructure (e.g., Mercier & Nicolas, 1975). However, similar structures are widely documented as melt-solid interaction and melt migration phenomena in exposed Phanerozoic mantle sections (e.g., Rampone et al., 2020). The recognition of former melt and significant transformation of microstructures in the studied mantle xenoliths poses the question of whether the melt is externally or locally derived (i.e., in an open or closed system). Next, we examine additional reaction textures to infer that the melt was externally derived and migrated through the cratonic mantle in a scenario of reactive flow.

The dominant microstructure of olivine (Ol_1) and orthopyroxene (Opx_1) is overprinted by symplectic clinopyroxene (Cpx_2) and vermicular spinel (Spl_1) (Fig. 5; see reactions R3 and R4 below). The overprinting relationship is shown by EBSD crystallographic orientation data where these symplectite minerals have topotaxic relationships with adjacent orthopyroxene (Opx_1) (Fig. 5c). Other crosscutting relationships include garnet films transecting orthopyroxene (Opx_1) grains (Fig. 6f; see reaction R5 below) and symplectic clinopyroxene (Cpx_3), garnet (Grt_2), olivine (Ol_2) and spinel (Spl_2) (Fig. 7a–c; see reaction R6 below). EBSD data also confirms a topotaxic relationship (Fig. 7e) between this final symplectite and orthopyroxene (Opx_1).

Origin of excess silica in cratonic peridotites

In his seminal paper, Boyd (1989) highlighted that olivine in the majority of coarse-grained cratonic peridotites tends to have very high forsterite content (Fig. 1b) and lower mode compared to its occurrence in oceanic peridotites. Walter (1998), in a comparative analysis between Si-rich cratonic peridotites and residues from isochemical partial melting experiments of pyrolite (3 to 7 GPa), highlighted the mismatch between the silica-rich experimental residues and cratonic peridotites (compare the yellow inverted triangles with peridotites at low olivine modes, Fig. 1b). Moreover, Walter (1998) pointed out that in the MgO/SiO_2 vs. SiO_2 space, the Si-rich peridotites (SiO_2 > 46 wt.%) form a trend towards higher orthopyroxene modes, similar to the reconstituted bulk rock compositions of the peridotites studied here (Table 2; Fig. 1c). The studied samples exhibit high SiO_2 content (up to 49.3 wt.%) and low MgO/SiO_2 ratios (0.85 to 0.91), reinforcing that they are not residues after isochemical partial melting (Walter, 1998).

Studies of the geometries and mineral assemblages of reaction zones in exposed sections of mantle peridotite (e.g., Quick, 1982) suggested that the channelised passage of melt through the upper mantle could significantly change the mode of the rock forming minerals, transforming lherzolite and harzburgite to dunite. Kelemen et al. (1992) expanded on this concept of melt-rock interaction in the transformation of lherzolite to harzburgite by comparing geochemical data for mantle peridotites with compositions of melts from lherzolite melting experiments. These authors concluded that reaction of the mantle lithosphere with ascending melts is widespread and changes the composition of the melt during ascent. The reaction also dissolves clinopyroxene, precipitates orthopyroxene, thereby increasing the silica content and changing the composition of the melt. In Alpine-Apennine ophiolites, Rampone et al. (2020) integrated microstructural observations and geochemical data to document open-system reactive porous flow causing dissolution and precipitation of olivine and orthopyroxene.

Kesson and Ringwood (1989) proposed that interaction between olivine and very Si-rich fluids derived from subduction-zones could have promoted the silica enrichment. We calculate hypothetical hybridisation scenarios of infiltration and reaction of four melts with refractory harzburgite (average SiO_2 of 43.8 wt.%; Table 2), to achieve the SiO_2 content (49.1 wt.%, Table 2) of the two most silica-rich samples studied (17BSK043 and 045). We investigated (i) a geologically implausible pure SiO_2 melt and more plausible melts including: (ii) tonalite-trondhjemite-granodiorite (TTG), (iii) sanukitoid (a granitoid with relatively high concentrations of compatible elements), and (iv) Cenozoic-modern boninite (Table 2). We find that infiltration and reaction of 9.6 wt.% of pure SiO_2 melt results in the required SiO_2 but lacks sufficient Cr_2O_3 and Al_2O_3 to match the observed peridotites. The more plausible melts with progressively lower SiO_2 contents, require mass fractions of 21 to 37 % of infiltrating melt, but, the resulting modified peridotite becomes overly enriched in incompatible elements such as TiO_2, K_2O and Na_2O, while remaining deficient in Cr_2O_3 (Table 2, Online Resource 5). Additionally, the bulk hybrid compositions used in the infiltration and reaction models presented by Tomlinson and Kamber (2021) and Walsh et al. (2023) are also overly enriched in Al_2O_3, FeO, and CaO (Online Resource 5).

The excessive enrichment in incompatible elements disqualifies the simple infiltration, reaction and freezing scenarios above. Instead, this suggests an open system of reactive melt flow (Kelemen et al., 1998) where preexisting peridotite lithosphere and the infiltrating melt react to form a solid enriched in orthopyroxene, with the modified melt escaping. Basalt-peridotite reaction produces high SiO_2 lherzolite residues too rich in clinopyroxene and with an olivine Fo-number too low to explain the studied xenoliths (Tomlinson & Kamber, 2021). In comparison, the komatiite-peridotite reaction also increases the SiO_2 content but produces orthopyroxene-rich harzburgites (Tomlinson & Kamber, 2021) and olivine of high Fo-content, particularly in the harzburgite-komatiite system (Fig. 9b). However, only an open system where the komatiite melt escapes can increase orthopyroxene modes to the extent (~30-55% orthopyroxene) required to match the studied xenoliths.

The garnet assemblages yielded equilibration *PT* of approximately 615–635°C and 2.4–2.9 GPa, suggesting that the 2–3 GPa thermodynamic model outputs of Tomlinson and Kamber (2021) and Walsh et al. (2023) are the most relevant to this study. Both thermodynamic models form orthopyroxene-rich harzburgite when melt is extracted at temperatures of 1546-1430°C (Fig. 9a) and 1623–1522°C (Fig. 9b). The higher temperature end of these ranges (i.e., #1 and #2 in Fig. 9a and b) are key for melt-rock interaction where the formation of high-silica harzburgite forms (i) high Mg# olivine and orthopyroxene, (ii) orthopyroxene in the absence of garnet and spinel (i.e., high Al and Cr), and (iii) the extremely low concentrations of incompatible Na and Ti in the rock, implying the escape of melt. This key silica-enrichment reaction matches that inferred from the microstructural evidence above. We extract the composition of the olivine plus orthopyroxene residue (i.e., averaged over the temperature range marked by #1 and #2 in Fig. 9a, b). These compositions (Ol+Opx solids #1 and #2 in Table 2) are plotted (red squares, Fig. 9c, d) and are broadly representative of the reaction products formed during high-temperature reactive flow of komatiite melt through the cratonic mantle at 2–3 GPa (reaction R1, purple text, Fig. 9).

Reaction R1:

$melt_{in}$ *(komatiite) + peridotite (assimilation of Grt/Spl ± Cpx)* $\rightarrow Ol_1 + Opx_1 + melt_{out}$

The mode of Opx_1 would be progressively increased with repetition of infiltration, high temperature reaction, within temperature ranges #1 and #2 (Fig. 9a and b) and escape of each batch of modified melt. With high time-integrated (i.e., aggregated) melt flux, this successively increases SiO_2 in the bulk rock composition. Rather than attempting to model this open-system with ad hoc assumptions about the escaped melt fractions, retained solid fractions and number of cycles, we constructed first-order mixing models (black dashed lines, Fig. 9c, d). For these, we mixed precursor refractory harzburgite (pink triangles, Fig. 9c, d, harzburgite residues after lherzolite (KR4003) melting in Table 2) and the extracted orthopyroxene (Opx_1) plus olivine (Ol_1) solid residues (red squares, Fig. 9c, d). The mixing lines show that the residues from the more refractory Walsh et al. (2023) model (#2) provide a closer fit to the studied samples for SiO_2 vs. MgO/SiO_2 (green symbols, Fig. 9c). This reflects the more magnesian nature of the residues in the harzburgite-komatiite system. The addition of approximately 50% orthopyroxene-dominated crystallisation products (red square #2, Fig. 9c, d) to highly refractory harzburgite (pink triangle #2, Table 2) yields to closest fit to the SiO_2 vs. MgO/SiO_2 trajectories (Fig. 9c). These simple models provide a plausible explanation for the origin of excess silica in cratonic peridotites. They also provide a good match for most other major elements (see Calculated Opx-enriched peridotite, Table 2).

A key feature of the high-temperature orthopyroxene formed in the infiltration and reaction models (Tomlinson & Kamber, 2021; Walsh et al., 2023) is their enrichment in Cr_2O_3. The simple mixing models between precursor peridotite (pink triangles, Fig. 9d) and increasing modes of high-temperature orthopyroxene (Opx_1) plus olivine (Ol_1) residues (red squares, Fig. 9d) also explain the high Cr_2O_3 of cratonic harzburgite compositions (i.e., excluding the high MgO/SiO_2 dunite samples, Fig. 9d). This Cr_2O_3 enrichment of cratonic harzburgite primarily arises from the precipitation of Cr-rich orthopyroxene and does not require the formation of chromian spinel which likely explains the high Cr_2O_3 of dunite (Fig. 9d). High Cr_2O_3 content is commonly found in orthopyroxene within coarse-grained spinel peridotites (e.g., Kopylova & Caro, 2004), distinguishing it from the less chromian pyroxene observed in garnet-bearing harzburgites (e.g., Ionov et al., 2010; Simon et al., 2007).

Furthermore, the enrichment of orthopyroxene and loss of melt maintains the significant depletion in incompatible elements (see Calculated Opx-enriched peridotite, Table 2). This depletion occurs because most of the TiO_2, K_2O and Na_2O partition into melt_{out} in reaction R1 and are subsequently transported upward through the lithosphere. The least well-matched element in the simple mixing model is Al (Al_2O_3=2.62–3.64, Table 2), with the natural peridotites having lower Al_2O_3 contents (0.73–1.68, Table 2). This discrepancy could reflect a combination of at least three issues.

Firstly, the analysed MgO-(Al_2O_3+Cr_2O_3) composition of orthopyroxene is variable due to lamellae (Fig. 8), shown by a nominally lower analytical reproducibility (Table 3). This variability points to the challenge of accurately estimating the concentration of Al_2O_3+Cr_2O_3+CaO in high-temperature orthopyroxene which contain spinel and clinopyroxene lamellae after cooling (Fig. 8b, c). Consequently, the reconstituted bulk rock calculations may inadvertently underestimate Al_2O_3 contents. Secondly, there is uncertainty in the activity-composition models for pyroxenes at very high temperatures, which may result in the thermodynamic models overestimating the Al_2O_3 content in high-temperature orthopyroxene. Lastly, if melt-solid interaction persisted to lower temperatures (discussed in the section ‘Near solidus reactions and model for symplectite formation’), it is possible that the high-temperature orthopyroxene re-equilibrated and lost some Al_2O_3+Cr_2O_3+CaO content to cooler melts that continued to migrate through the lithosphere after the bulk of high-temperature orthopyroxene had formed.

In summary, we propose that komatiite melts with relatively modest SiO_2 content (46.5 to 48.5 wt%), originating from greater depths (e.g., 7–10 GPa), migrated through and reacted with pre-existing harzburgite cratonic lithosphere. Deeply sourced komatiite liquids are orthopyroxene-saturated at > 2.5 GPa (Online Resource 2 – Supplementary Figure 4) because they derive from low SiO_2 garnet-dunite residues. While crystallisation of such liquids within the cratonic lithosphere would create very orthopyroxene-rich rocks, their Mg# would be much lower than that observed in Si-rich peridotites. The existing evidence suggests that the Kaapvaal proto-cratonic lithosphere was already very deep (>200 km: e.g., Hoare et al., 2022) in the Archaean. Therefore, rising deep komatiite melt would encounter refractory harzburgite at the lithosphere-asthenosphere boundary (LAB). Melt-solid reaction there shifts saturation from orthopyroxene to olivine (Online Resource 2 – Supplementary Figure 4) and increases the Mg# of the melt. In an open system, the reactive passage of komatiite could cause some melt loss and olivine crystallisation, which would evolve the melt to higher SiO_2. Such deep (4-6 GPa) melt-solid interaction could explain the SiO_2-poor, high MgO/SiO_2 peridotites plotting to the left of closed-system residues in Figures 1c and 9c.

Reaction of rising evolved komatiite melt with shallower (<4 GPa) harzburgite then precipitated dominantly orthopyroxene (Opx_1), but as seen with the mutual apparent inclusions, also some olivine. As the bronzitic harzburgite xenoliths make up only 5–10% of the total peridotites at the Bultfontein pans, we interpret that komatiite melt migration forming the studied xenoliths occurred in channels, matching mafic and ultramafic eruption centres in greenstone belts. This new model of a predominance of orthopyroxene precipitation during high-temperature open system reactive flow is strongly supported by the multiple lines of microstructural evidence for former melt in the peridotites studied here. Therefore, assemblages in Si-rich cratonic peridotites reflect channels of melt-solid interaction between ascending evolved komatiite melt and pre-existing lithospheric mantle. The interaction modifies the melt composition from high MgO/SiO_2 to low MgO/SiO_2 komatiite (Fig. 9b) and eventually to high-MgO basalt (Fig. 9a and b).

Near solidus reactions and model for symplectite formation

Clinopyroxene (Cpx_1) occurs in both harzburgite and lherzolite as interstitial films between olivine and orthopyroxene (Fig. 2a inset and Fig. 6). These films have been observed in other mantle peridotites (e.g., Kopylova & Caro, 2004; Simon et al., 2007). This texture is replicated in the infiltration and reaction model (section 2, Fig. 9a) of Tomlinson and Kamber (2021) forming inferred reaction 2.

Reaction R2:

$melt_{in}$ *(high-MgO basalt)* + $Opx_1 \rightarrow Cpx_1 + Ol_1 + melt_{out}$

Clinopyroxene (Cpx_2) occurs in both harzburgite and lherzolite as vermicular intergrowths with spinel (Fig. 5). These symplectites (0.5 to 2.5 mm across) are nearly exclusively found along curved orthopyroxene-orthopyroxene-olivine or orthopyroxene-olivine-olivine grain boundaries (Figs. 2b and 3a). They mostly protrude away from orthopyroxene into adjacent olivine and/or between olivine grain boundaries (Fig. 2b). Within a symplectite, the clinopyroxene and spinel each exhibit a single crystallographic orientation (Fig. 5), a common feature in vermicular intergrowths (e.g., Obata & Ozawa, 2011; Xu et al., 2015). Moreover, EBSD data reveal topotaxic relationships between the symplectite and the adjacent orthopyroxene, where the minerals in the symplectite nucleate their orientations based on nearby orthopyroxene (Opx_1) in the studied samples. The preservation of these symplectites since the Archaean is likely due to their low strain, low fluid infiltration history, along with a lack of other aluminous phases to re-equilibrate with (e.g. spinel is the only Al phase in the harzburgites). This symplectite texture is replicated in the infiltration and reaction model (sections 3 and 4, Fig. 9a) of Tomlinson and Kamber (2021) forming inferred reactions 3 and 4.

Reaction R3:

$melt_{in}$ *(high-MgO basalt)* + $Opx_1 \rightarrow Cpx_2 + Spl_1 + melt_{out}$

Reaction R4:

$melt_{in}$ *(high-MgO basalt)* + $Opx_1 + Ol_1 \rightarrow Cpx_2 + Spl_1 + melt_{out}$

Although these clinopyroxene and spinel symplectites are commonly found in nominally garnet-free cratonic peridotites (e.g., Field & Haggerty, 1994; Simon et al., 2007), they are relatively poorly documented and understood. Two contrasting origins have been proposed: (1) sub-solidus exsolution of clinopyroxene (Ca-Al-Cr) from high-temperature orthopyroxene, diffusive migration of Cr-rich clinopyroxene to grain boundaries, and unmixing to form the symplectite (e.g., Field & Haggerty, 1994; Obata & Ozawa, 2011; Simon et al., 2007), and (2) melt-olivine reaction forming the symplectite (e.g., Suhr et al., 2008). Suhr et al. (2008) rejected the exsolution hypothesis from a Ca-

Al-Cr-rich pyroxene (origin 1 above) based on mass balance considerations, finding that the precursor pyroxene would have an implausibly high Cr_2O_3 content of ~12 wt%. Calculations for symplectites from the Kaapvaal craton have equally implausible reintegrated Cr_2O_3 contents of 9–29 wt% (table 10 of Field, 2008). Release of Cr from the breakdown of high-temperature orthopyroxene (sections 2–4, Fig. 9a) will enrich the high-MgO basaltic melt in Cr_2O_3, supplying Cr to the symplectites.

In the studied samples, we suggest a melt-olivine reaction forming the symplectite (origin 2 above) as lamellae-free orthopyroxene is very rare and small. Instead, both clinopyroxene and spinel lamellae (i.e., exsolutions) are ubiquitous with uniform mode across each coarse orthopyroxene grain (Fig. 8b, c), precluding migration of Ca-Al-Cr-rich clinopyroxene towards grain edges (origin 1 above). This is supported by (i) the chemical uniformity of the orthopyroxene (Table 3), including in CaO, Al_2O_3 and Cr_2O_3; (ii) the irregular distribution of the symplectites (Fig. 3a), similar to observations in oceanic harzburgites and dunites (Suhr et al., 2008), (iii) the size of the symplectites compared to adjacent orthopyroxene grain sizes (e.g., the symplectite in Fig. 2b), and (iv) the clinopyroxene films (Cpx_1) near symplectites (17BSK039, 040 and 045) have lamellae (e.g., Fig. 8d) and did not unmix into a symplectite.

Garnet (Grt_1) occurs in two lherzolite samples as interstitial films along orthopyroxene grain boundaries and cutting across orthopyroxene grains (Fig. 6f). This texture has been explained by sub-solidus exsolution from orthopyroxene (e.g., Cox, 1987; Gibson, 2017; Tomlinson et al., 2018). However, in the samples studied here, garnet films occur both along orthopyroxene grain boundaries and cutting across orthopyroxene (Fig. 6), suggesting a role for melt-rock interaction, as replicated in the infiltration and reaction model (section 5, Fig. 9b) of Walsh et al. (2023) forming inferred reaction 5.

Reaction R5:

$melt_{in}$ *(komatiite)* $\rightarrow Ol_1 + Opx_1 + Grt_1 + melt_{out}$

In addition to the clinopyroxene-spinel symplectites formed by reactions 3 and 4, some lherzolite samples (17BSK039 and 040) also have complex symplectites containing garnet (Grt_2), clinopyroxene (Cpx_3), spinel (Spl_2), and olivine (Ol_2) (Fig. 7), a texture previously noted by Field (2008) and Field and Haggerty (1994). These symplectites (<3 mm across) have ragged boundaries and are found at olivine-olivine, orthopyroxene-olivine-olivine and orthopyroxene-clinopyroxene-olivine grain boundaries (Fig. 6a). They mostly protrude into adjacent olivine (Fig. 6a). Clinopyroxene (Cpx_3) associated with garnet lacks visible lamellae, suggesting a lower temperature formation. Within a symplectite, the clinopyroxene and spinel each exhibit several crystallographic orientations (Fig. 7, Online Resource 2 – Supplementary Figure 3). Moreover, EBSD data reveal topotaxic relationships between the symplectite and the adjacent orthopyroxene and olivine. Some relict olivine (Ol_1) is observed within the symplectite in addition to new olivine (Ol_2, Fig. 7d). Current thermodynamic activity-composition models do not yet allow reliable calculations for co-existing spinel and garnet. However, this second symplectite texture is similar to the infiltration and reaction model (section 6, Fig. 9b) of Walsh et al. (2023) forming inferred reaction 6.

Reaction R6:

$melt_{in}$ *(komatiitic basalt)* $+ Opx_1 \rightarrow Ol_2 + Cpx_3 + Grt_2 + Spl_2 + melt_{out}$

Reaction 6 (1520–1499°C) occurs just above the solidus (section 6, Fig. 9a), where the komatiitic melt had fractionated to a komatiitic basalt composition. Similar to the clinopyroxene-spinel symplectites, these garnet-bearing symplectites have very low concentrations of TiO_2 and K_2O (Tables 2, 4 and 5), indicating that the external melt evolved further and that at least some of it escaped. The near solidus reaction temperature is supported by low Cr_2O_3 (1.0 – 1.1 wt%) in garnet (Walsh et al., 2023), distinct from high-temperature garnet in garnet peridotites (Cr2O3 = 4–12 wt%; e.g., Kopylova & Caro, 2004).

In some samples (17BSK039, 040 and 044), amphibole films (Fig. 7a; Table 5) suggest an additional stage of even lower temperature interaction between peridotite and the most evolved fraction of melt. Texturally and chemically similar K-poor amphibole was described by Field and Haggerty (1994) from Kaapvaal peridotites. The low TiO_2 and K_2O of the amphiboles precludes the melt from being a potassic and volatile-rich metasomatic agent, which would form K-rich richterite, phlogopite, and apatite reaction products (e.g., Kramers et al., 1983).

In summary, microstructural and chemical mass balance evidence combined with a reasonable match with thermodynamic infiltration and reaction models supports a continuum scenario of melt-rock interaction during reactive melt flow. This is similar to reactive melt percolation models for pyroxenite layers in depleted ophiolite peridotites (e.g., Basch et al., 2019; Rampone et al., 2008).

Implications for the evolution of Archaean cratonic lithosphere

The reactions between post-Archaean melts and cratonic mantle have been well documented in many xenoliths studies (e.g. reactions between xenoliths and host kimberlite melts), detailing the mineralogical, geochemical, and isotopic changes (e.g., Aulbach et al., 2013; Dawson, 2002; Griffin et al., 1999; Konzett et al., 2000; Kramers et al., 1983). These studies generally agree that metasomatism occurred over extended periods and involved melts or fluids of enriched compositions (e.g., lowering Mg-numbers and introducing phlogopite and K-richterite). The findings of this study into Archaean melt-rock interactions (i.e., Si-enrichment metasomatism) provide new insights that differ from previous studies in two ways: (1) the silica-rich and incompatible element-poor character of bulk compositions of the studied samples indicate reactive flow of komatiite melt which evolves to a high-MgO basalt, consistent with thermodynamic modelling research (e.g., Tomlinson & Kamber, 2021), and (2) the microstructural evidence and the modal abundances indicate that orthopyroxene-rich peridotites formed from high time-integrated melt flux at high temperatures.

While rare tabular pyroxenite has been described in cratonic peridotite (e.g., Bell et al., 2005; Chin et al., 2020), this and other studies (e.g., Baptiste et al., 2012; Simon et al., 2007) suggest channelised porous flow of melt through Archaean cratonic lithosphere was a common process. Specifically, high time-integrated melt flux of komatiite removes the need for models invoking highly silicic melts (e.g., Canil & Lee, 2009; Kesson & Ringwood, 1989; Wasch et al., 2009) to produce excess orthopyroxene (Bénard et al., 2021; Nishio et al., 2023) and explains the standard mantle O-isotope compositions of cratonic mantle (Regier et al., 2018). Additionally, a reactive flow model explains the complex trace element patterns of many refractory cratonic peridotites. While depleted in many incompatible trace elements (e.g., Ti, Th, U), their rare earth element patterns (e.g., Bell et al., 2005; Gibson et al., 2013; Tomlinson et al., 2018), suggest interaction with deep komatiitic melts from the mantle transition zone (e.g., Corgne et al., 2005; McKenzie, 2020; Pierru et al., 2022; Wyman, 2018).

Several mechanisms could have aided the diffuse porous melt flow identified in this study, including the advection of the melting mantle, heat pipes, porosity waves in heated lithosphere, or mantle overturn upwelling zones (Bédard, 2018; Bessat et al., 2022; Moore & Webb, 2013). Evidence of Al-rich olivine xeno- or antecrysts in the 3.3 Ga Commondale komatiite supports these models (Wilson & Bolhar, 2022).

Seismic studies indicate that cratons are layered with near-horizontal azimuthal anisotropies, particularly at the depth of spinel stability (e.g., Chen et al., 2021; Snyder & Bruneton, 2007; Sodoudi et al., 2013). This anisotropy, often attributed to olivine and orthopyroxene CPO, suggests sub-horizontal deformation and compositional layering dating back to craton assembly. However, the samples studied here are coarse-grained, low-strain rocks with weak fabrics and low SPO. In our EBSD maps, the number of grains was too low to investigate CPO in a statistically robust manner, making it difficult to assess models of lithospheric seismic anisotropy. When calculating seismic anisotropy from mantle xenolith samples a statistically valid CPO is needed. Future work should ensure that the CPO, using one point per grain, is determined from EBSD data collected on more than 150 grains (Skemer et al., 2005).

Nonetheless, the slip system activity can still be derived on fewer grains using subgrain boundary analysis IPFs (Fig. 4). This method can provide an indication of the large-scale CPO and, consequently, the seismic anisotropy as suggested by Bernard et al. (2021). It is important to note that the strength of the anisotropy cannot be reliably assessed. However, the samples analysed here do not show alignment of the olivine a-axis commonly found in deformed peridotites (Bernard et al., 2021) suggesting these bronzitic peridotites are atypical of the mantle. Additionally, if the melt flow is channelised as proposed here, the studied spinel facies samples may not be visible in seismic studies as they form only 5-10% of the mantle lithosphere.

In summary, the reactive flow of komatiitic melts with pre-existing lithospheric mantle, involving high time-integrated melt flux, played a crucial role in the evolution of cratonic peridotites and eruption of komatiite and high-MgO basalt during the Archaean. Further research is needed to fully understand the implications of reactive flow for the geodynamic evolution of cratonic lithosphere, compositional variations in komatiites and high-MgO basalts, melt-rock interactions in the garnet facies, and integration of these processes over the entire transgressed lithosphere.

Summary

All the studied coarse-grained, high-silica peridotites (orthopyroxene up to 55 vol.%) contain microstructural evidence for the former presence of melt, including low apparent dihedral angles, irregular high-energy grain boundaries, neighbourhoods of apparently separate grains of olivine and orthopyroxene which are likely a single grain connected in 3D, and extremely elongate grains. These microstructures form during reactive flow and represent crystallised grain boundary melt networks.

The studied samples are highly refractory with olivine Fo-contents of 92.9±0.3, reconstituted whole rock Mg-number of 92.9 ±0.4 and negligible TiO_2 concentrations. We attribute these chemical characteristics to reactive melt flow of komatiite melt through pre-existing, proto-cratonic lithosphere with high time-integrated melt flux, negating the need for a Si-rich melt. The most orthopyroxene-rich samples represent melt passage channels that have seen a continuum of reactive flow from very high-temperature orthopyroxene precipitation to interstitial clinopyroxene-spinel symplectite formation. Melt-rock interaction and reactive flow also modifies the migrating komatiite melt, suggesting in addition to melt-rock interactions, that melt evolution in Archean channels is also an important process in the formation of the Archean cratons.

Data availability

The authors confirm that the data supporting the findings of this study are available within tables and the Online Resources.

References

Acevedo Zamora, M. A., & Kamber, B. S. (2023). Petrographic microscopy with ray tracing and segmentation from multi-angle polarisation whole-slide images. *Minerals*, *13*(2), 156. https://doi.org/10.3390/min13020156

Aulbach, S., Griffin, W. L., Pearson, N. J., & O'Reilly, S. Y. (2013). Nature and timing of metasomatism in the stratified mantle lithosphere beneath the central Slave craton (Canada). *Chemical Geology*, *352*, 153-169. https://doi.org/10.1016/j.chemgeo.2013.05.037

Aulbach, S., Griffin, W. L., Pearson, N. J., O'Reilly, S. Y., Kivi, K., & Doyle, B. J. (2004). Mantle formation and evolution, Slave Craton: constraints from HSE abundances and Re–Os isotope systematics of sulfide inclusions in mantle xenocrysts. *Chemical Geology*, *208*(1-4), 61-88. https://doi.org/10.1016/j.chemgeo.2004.04.006

Baptiste, V., Tommasi, A., & Demouchy, S. (2012). Deformation and hydration of the lithospheric mantle beneath the Kaapvaal craton, South Africa. *Lithos*, *149*, 31-50. https://doi.org/10.1016/j.lithos.2012.05.001

Basch, V., Rampone, E., Borghini, G., Ferrando, C., & Zanetti, A. (2019). Origin of pyroxenites in the oceanic mantle and their implications on the reactive percolation of depleted melts. *Contributions to Mineralogy and Petrology*, *174*, 1-25. https://doi.org/10.1007/s00410-019-1640-0

Bascou, J., Doucet, L. S., Saumet, S., Ionov, D. A., Ashchepkov, I. V., & Golovin, A. V. (2011). Seismic velocities, anisotropy and deformation in Siberian cratonic mantle: EBSD data on xenoliths from the Udachnaya kimberlite. *Earth and Planetary Science Letters*, *304*(1-2), 71-84. https://doi.org/10.1016/j.epsl.2011.01.016

Bédard, J. H. (2018). Stagnant lids and mantle overturns: Implications for Archaean tectonics, magmagenesis, crustal growth, mantle evolution, and the start of plate tectonics. *Geoscience Frontiers*, *9*(1), 19-49. https://doi.org/10.1016/j.gsf.2017.01.005

Bell, D. R., Gregoire, M., Grove, T., Chatterjee, N., Carlson, R., & Buseck, P. (2005). Silica and volatile-element metasomatism of Archean mantle: a xenolith-scale example from the Kaapvaal Craton. *Contributions to Mineralogy and Petrology*, *150*, 251-267. https://doi.org/10.1007/s00410-005-0673-8

Bénard, A., Müntener, O., Pilet, S., Arculus, R., & Nebel, O. (2021). Silica-rich spinel harzburgite residues formed by fractional hybridization-melting of the intra-oceanic supra-subduction zone mantle: new evidence from TUBAF seamount peridotites. *Geochimica et Cosmochimica Acta*, *293*, 477-506. https://doi.org/10.1016/j.gca.2020.11.001

Bernard, R. E., Schulte-Pelkum, V., & Behr, W. M. (2021). The competing effects of olivine and orthopyroxene CPO on seismic anisotropy. *Tectonophysics*, *814*, 228954. https://doi.org/10.1016/j.tecto.2021.228954

Bessat, A., Pilet, S., Podladchikov, Y. Y., & Schmalholz, S. M. (2022). Melt migration and chemical differentiation by reactive porosity waves. *Geochemistry, Geophysics, Geosystems*, *23*(2), e2021GC009963. https://doi.org/10.1029/2021GC009963

Boullier, A. M., & Nicolas, A. (1975). Classification of textures and fabrics of peridotite xenoliths from South African kimberlites. In *Physics and Chemistry of the Earth* (pp. 467-475). Elsevier. https://doi.org/10.1016/B978-0-08-018017-5.50037-7

Boyce, A., Bodin, T., Durand, S., Soergel, D., & Debayle, E. (2024). Seismic evidence for craton formation by underplating and development of the MLD. *Geophysical Research Letters*, *51*(4), e2023GL106170. https://doi.org/10.1029/2023GL106170

Boyd, F. (1989). Compositional distinction between oceanic and cratonic lithosphere. *Earth and Planetary Science Letters*, *96*(1-2), 15-26. https://doi.org/10.1016/0012-821X(89)90120-9

Boyd, F., & Nixon, P. (1973). Origin of the lherzolite nodules in the kimberlites of Northern Lesotho. International Kimberlite Conference: Extended Abstracts,

Canil, D., & Lee, C.-T. A. (2009). Were deep cratonic mantle roots hydrated in Archean oceans? *Geology*, *37*(7), 667-670. https://doi.org/10.1130/G25610A.1

Chen, X., Levin, V., Yuan, H., Klaser, M., & Li, Y. (2021). Seismic anisotropic layering in the Yilgarn and Superior cratonic lithosphere. *Journal of Geophysical Research: Solid Earth*, *126*(8), e2020JB021575. https://doi.org/10.1029/2020JB021575

Chin, E. J., Soustelle, V., & Liu, Y. (2020). An SPO-induced CPO in composite mantle xenoliths correlated with increasing melt-rock interaction. *Geochimica et Cosmochimica Acta*, *278*, 199-218. https://doi.org/10.1016/j.gca.2019.10.002

Condie, K. C. (1993). Chemical composition and evolution of the upper continental crust: Contrasting results from surface samples and shales. *Chemical Geology*, *104*(1), 1-37. https://doi.org/10.1016/0009-2541(93)90140-E

Condie, K. C. (1998). Episodic continental growth and supercontinents: a mantle avalanche connection? *Earth and Planetary Science Letters*, *163*(1-4), 97-108. https://doi.org/10.1016/S0012-821X(98)00178-2

Corgne, A., Liebske, C., Wood, B. J., Rubie, D. C., & Frost, D. J. (2005). Silicate perovskite-melt partitioning of trace elements and geochemical signature of a deep perovskitic reservoir. *Geochimica et Cosmochimica Acta*, *69*(2), 485-496. https://doi.org/10.1016/j.gca.2004.06.041

Cox, K. G., Smith M. R., Beswetherick, S. (1987). Textural studies of garnet lherzolites: evidence of exsolution origin from high-temperature harzburgites. In P. H. Nixon (Ed.), *Mantle xenoliths* (pp. 537-550). John Wiley & Sons. https://doi.org/10.1002/gj.3350240214

Daczko, N. R., & Piazolo, S. (2022). Recognition of melferite–A rock formed in syn-deformational high-strain melt-transfer zones through sub-solidus rocks: A review and synthesis of microstructural criteria. *Lithos*, 106850. https://doi.org/10.1016/j.lithos.2022.106850

Dawson, J. (2002). Metasomatism and partial melting in upper-mantle peridotite xenoliths from the Lashaine volcano, northern Tanzania. *Journal of Petrology*, *43*(9), 1749-1777. https://doi.org/10.1093/petrology/43.9.1749

DIGIS Team. (2021). *GEOROC Compilation: Rock Types*. https://doi.org/https://doi.org/10.25625/2JETOA

Emo, R. B., & Kamber, B. S. (2022). Linking granulites, intraplate magmatism, and bi-mineralic eclogites with a thermodynamic-petrological model of melt-solid interaction at the base of anorogenic lower continental crust. *Earth and Planetary Science Letters*, *594*, 117742.

Ferracutti, G. R., Gargiulo, M. F., Ganuza, M. L., Bjerg, E. A., & Castro, S. M. (2015). Determination of the spinel group end-members based on electron microprobe analyses. *Mineralogy and Petrology*, *109*, 153-160. https://doi.org/10.1007/s00710-014-0363-1

Field, S. W. (2008). Diffusion, discontinuous precipitation, metamorphism, and metasomatism: The complex history of South African upper-mantle symplectites. *American mineralogist*, *93*(4), 618-631. https://doi.org/10.2138/am.2008.2626

Field, S. W., & Haggerty, S. E. (1994). Symplectites in upper mantle peridotites: development and implications for the growth of subsolidus garnet, pyroxene and spinel. *Contributions to Mineralogy and Petrology*, *118*, 138-156. https://doi.org/10.1007/BF01052865

Gibson, S., McMahon, S., Day, J., & Dawson, J. (2013). Highly refractory lithospheric mantle beneath the Tanzanian craton: evidence from Lashaine pre-metasomatic garnet-bearing peridotites. *Journal of Petrology*, *54*(8), 1503-1546. https://doi.org/10.1093/petrology/egt020

Gibson, S. A. (2017). On the nature and origin of garnet in highly-refractory Archean lithospheric mantle: Constraints from garnet exsolved in Kaapvaal craton orthopyroxenes. *Mineralogical magazine*, *81*(4), 781-809. https://doi.org/10.1180/minmag.2016.080.158

Griffin, S., Daly, L., Keller, T., Piazolo, S., Forman, L. V., Lee, M. R., Baumgartner, R. J., Trimby, P. W., Benedix, G. K., & Irving, A. J. (2022). Constraints on the emplacement of Martian nakhlite igneous rocks and their source volcano from advanced micro-petrofabric analysis. *Journal of Geophysical Research: Planets*, *127*(6), e2021JE007080. https://doi.org/10.1029/2021JE007080

Griffin, W., O'Reilly, S., Abe, N., Aulbach, S., Davies, R., Pearson, N., Doyle, B., & Kivi, K. (2003). The origin and evolution of Archean lithospheric mantle. *Precambrian Research*, *127*(1-3), 19-41. https://doi.org/10.1016/S0301-9268(03)00180-3

Griffin, W., Shee, S., Ryan, C., Win, T., & Wyatt, B. (1999). Harzburgite to lherzolite and back again: metasomatic processes in ultramafic xenoliths from the Wesselton kimberlite, Kimberley, South Africa. *Contributions to Mineralogy and Petrology*, *134*(2), 232-250. https://doi.org/10.1007/s004100050481

Heilimo, E., Halla, J., & Hölttä, P. (2010). Discrimination and origin of the sanukitoid series: geochemical constraints from the Neoarchean western Karelian Province (Finland). *Lithos*, *115*(1-4), 27-39. https://doi.org/10.1016/j.lithos.2009.11.001

Hoare, B. C., Tomlinson, E. L., & Kamber, B. S. (2022). Evidence for a very thick Kaapvaal craton root: Implications for equilibrium fossil geotherms in the early continental lithosphere. *Earth and Planetary Science Letters*, *597*, 117796. https://doi.org/10.1016/j.epsl.2022.117796

Ionov, D. A., Doucet, L. S., & Ashchepkov, I. V. (2010). Composition of the lithospheric mantle in the Siberian craton: new constraints from fresh peridotites in the Udachnaya-East kimberlite. *Journal of Petrology*, *51*(11), 2177-2210. https://doi.org/10.1093/petrology/egq053

Kamber, B. S., & Tomlinson, E. L. (2019). Petrological, mineralogical and geochemical peculiarities of Archaean cratons. *Chemical Geology*, *511*, 123-151.

Kelemen, P. B., Dick, H. J., & Quick, J. E. (1992). Formation of harzburgite by pervasive melt/rock reaction in the upper mantle. *Nature*, *358*(6388), 635-641. https://doi.org/10.1038/358635a0

Kelemen, P. B., Hart, S. R., & Bernstein, S. (1998). Silica enrichment in the continental upper mantle via melt/rock reaction. *Earth and Planetary Science Letters*, *164*(1-2), 387-406. https://doi.org/10.1016/S0012-821X(98)00233-7

Kesson, S. E., & Ringwood, A. E. (1989). Slab-mantle interactions: 2. The formation of diamonds. *Chemical Geology*, *78*(2), 97-118. https://doi.org/10.1016/0009-2541(89)90109-5

Konzett, J., Armstrong, R. A., & Günther, D. (2000). Modal metasomatism in the Kaapvaal craton lithosphere: constraints on timing and genesis from U–Pb zircon dating of metasomatized peridotites and MARID-type xenoliths. *Contributions to Mineralogy and Petrology*, *139*(6), 704-719. https://doi.org/10.1007/s004100000160

Kopylova, M., & Caro, G. (2004). Mantle xenoliths from the southeastern Slave craton: evidence for chemical zonation in a thick, cold lithosphere. *Journal of Petrology*, *45*(5), 1045-1067. https://doi.org/10.1093/petrology/egh003

Kramers, J., Roddick, J., & Dawson, J. (1983). Trace element and isotope studies on veined, metasomatic and “MARID” xenoliths from Bultfontein, South Africa. *Earth and Planetary Science Letters*, *65*(1), 90-106. https://doi.org/10.1016/0012-821X(83)90192-9

Le Bas, M., & Streckeisen, A. L. (1991). The IUGS systematics of igneous rocks. *Journal of the Geological Society*, *148*(5), 825-833. https://doi.org/10.1144/gsjgs.148.5.0825

Le Roux, V., Bodinier, J.-L., Tommasi, A., Alard, O., Dautria, J.-M., Vauchez, A., & Riches, A. (2007). The Lherz spinel lherzolite: refertilized rather than pristine mantle. *Earth and Planetary Science Letters*, *259*(3-4), 599-612.

McKenzie, D. (2020). Speculations on the generation and movement of komatiites. *Journal of Petrology*, *61*(7), egaa061. https://doi.org/10.1093/petrology/egaa061

Mercier, J. C., & Nicolas, A. (1975). Textures and fabrics of upper-mantle peridotites as illustrated by xenoliths from basalts. *Journal of Petrology*, *16*(1), 454-487. https://doi.org/10.1093/petrology/16.1.454

Moore, W. B., & Webb, A. A. G. (2013). Heat-pipe earth. *Nature*, *501*(7468), 501-505. https://doi.org/10.1038/nature12473

Nimis, P., & Taylor, W. R. (2000). Single clinopyroxene thermobarometry for garnet peridotites. Part I. Calibration and testing of a Cr-in-Cpx barometer and an enstatite-in-Cpx thermometer. *Contributions to Mineralogy and Petrology*, *139*, 541-554. https://doi.org/10.1007/s004100000156

Nishio, I., Morishita, T., Tamura, A., Itano, K., Takamizawa, S., Ichiyama, Y., Arai, S., Barrett, N., & Szilas, K. (2023). Formation of Ultra-Depleted Mantle Peridotites and Their Relationship With Boninitic Melts: An Example From the Kamuikotan Unit, Hokkaido, Japan. *Journal of Geophysical Research: Solid Earth*, *128*(2), e2022JB025066. https://doi.org/10.1029/2022JB025066

Obata, M., & Ozawa, K. (2011). Topotaxic relationships between spinel and pyroxene in kelyphite after garnet in mantle-derived peridotites and their implications to reaction mechanism and kinetics. *Mineralogy and Petrology*, *101*, 217-224. https://doi.org/10.1007/s00710-011-0145-y

Pearson, D., Carlson, R., Shirey, S., Boyd, F., & Nixon, P. (1995). Stabilisation of Archaean lithospheric mantle: A ReOs isotope study of peridotite xenoliths from the Kaapvaal craton. *Earth and Planetary Science Letters*, *134*(3-4), 341-357. https://doi.org/10.1016/0012-821X(95)00125-V

Pearson, D., Shirey, S., Bulanova, G., Carlson, R., & Milledge, H. (1999). Re-Os isotope measurements of single sulfide inclusions in a Siberian diamond and its nitrogen aggregation systematics. *Geochimica et Cosmochimica Acta*, *63*(5), 703-711. https://doi.org/10.1016/S0016-7037(99)00042-3

Pearson, D. G., Scott, J. M., Liu, J., Schaeffer, A., Wang, L. H., van Hunen, J., Szilas, K., Chacko, T., & Kelemen, P. B. (2021). Deep continental roots and cratons. *Nature*, *596*(7871), 199-210. https://doi.org/10.1038/s41586-021-03600-5

Pierru, R., Andrault, D., Manthilake, G., Monteux, J., Devidal, J. L., Guignot, N., King, A., & Henry, L. (2022). Deep mantle origin of large igneous provinces and komatiites. *Science advances*, *8*(44), eabo1036. https://doi.org/10.1126/sciadv.abo10

Pike, J. E., Meyer, C., & Wilshire, H. (1977). Lashaine, Tanzania xenoliths: a new collection. International Kimberlite Conference: Extended Abstracts,

Quick, J. E. (1982). The origin and significance of large, tabular dunite bodies in the Trinity peridotite, northern California. *Contributions to Mineralogy and Petrology*, *78*(4), 413-422. https://doi.org/10.1007/BF00375203

Rampone, E., Borghini, G., & Basch, V. (2020). Melt migration and melt-rock reaction in the Alpine-Apennine peridotites: Insights on mantle dynamics in extending lithosphere. *Geoscience Frontiers*, *11*(1), 151-166. https://doi.org/10.1016/j.gsf.2018.11.001

Rampone, E., Piccardo, G. B., & Hofmann, A. W. (2008). Multi-stage melt–rock interaction in the Mt. Maggiore (Corsica, France) ophiolitic peridotites: microstructural and geochemical evidence. *Contributions to Mineralogy and Petrology*, *156*, 453-475. https://doi.org/10.1007/s00410-008-0296-y

Regier, M., Miškovic, A., Ickert, R. B., Pearson, D. G., Stachel, T., Stern, R. A., & Kopylova, M. (2018). An oxygen isotope test for the origin of Archean mantle roots. *Geochemical Perspectives Letters*, *9*, 6-10. https://doi.org/10.7185/geochemlet.1830

Riel, N., Kaus, B. J., Green, E., & Berlie, N. (2022). MAGEMin, an efficient Gibbs energy minimizer: application to igneous systems. *Geochemistry, Geophysics, Geosystems*, *23*(7), e2022GC010427.

Ruzicka, A. M., & Hugo, R. C. (2018). Electron backscatter diffraction (EBSD) study of seven heavily metamorphosed chondrites: Deformation systematics and variations in pre-shock temperature and post-shock annealing. *Geochimica et Cosmochimica Acta*, *234*, 115-147. https://doi.org/10.1016/j.gca.2018.05.014

Simon, N. S., Carlson, R. W., Pearson, D. G., & Davies, G. R. (2007). The origin and evolution of the Kaapvaal cratonic lithospheric mantle. *Journal of Petrology*, *48*(3), 589-625. https://doi.org/10.1093/petrology/egl074

Skemer, P., Katayama, I., Jiang, Z., & Karato, S.-i. (2005). The misorientation index: Development of a new method for calculating the strength of lattice-preferred orientation. *Tectonophysics*, *411*(1–4), 157-167. https://doi.org/http://dx.doi.org/10.1016/j.tecto.2005.08.023

Smith, C. B., Pearson, D. G., Bulanova, G. P., Beard, A. D., Carlson, R. W., Wittig, N., Sims, K., Chimuka, L., & Muchemwa, E. (2009). Extremely depleted lithospheric mantle and diamonds beneath the southern Zimbabwe Craton. *Lithos*, *112*, 1120-1132. https://doi.org/10.1016/j.lithos.2009.05.013

Snyder, D., & Bruneton, M. (2007). Seismic anisotropy of the Slave craton, NW Canada, from joint interpretation of SKS and Rayleigh waves. *Geophysical Journal International*, *169*(1), 170-188. https://doi.org/10.1111/j.1365-246X.2006.03287.x

Sodoudi, F., Yuan, X., Kind, R., Lebedev, S., Adam, J. M. C., Kästle, E., & Tilmann, F. (2013). Seismic evidence for stratification in composition and anisotropic fabric within the thick lithosphere of Kalahari Craton. *Geochemistry, Geophysics, Geosystems*, *14*(12), 5393-5412. https://doi.org/10.1002/2013GC004955

Stachel, T. (2022). *PTEXL - Geothermobarometry of Mantle Rocks* Version V2) Borealis. https://doi.org/doi:10.5683/SP3/IMYNCL

Stuart, C. A., Piazolo, S., & Daczko, N. R. (2018). The recognition of former melt flux through high-strain zones. *Journal of Metamorphic Geology*, *36*(8), 1049-1069. https://doi.org/doi:10.1111/jmg.12427

Sudholz, Z. J., Yaxley, G. M., Jaques, A. L., & Brey, G. P. (2021). Experimental recalibration of the Cr-in-clinopyroxene geobarometer: improved precision and reliability above 4.5 GPa. *Contributions to Mineralogy and Petrology*, *176*, 1-20. https://doi.org/10.1007/s00410-020-01768-z

Suhr, G., Kelemen, P., & Paulick, H. (2008). Microstructures in Hole 1274A peridotites, ODP Leg 209, Mid-Atlantic Ridge: Tracking the fate of melts percolating in peridotite as the lithosphere is intercepted. *Geochemistry, Geophysics, Geosystems*, *9*(3). https://doi.org/10.1029/2007GC001726

Taylor, W. R. (1998). An experimental test of some geothermometer and geobarometer formulations for upper mantle peridotites with applicaton to the thermobarometry of fertile lherzolite and garnet webserite. *Neues Jahrbuch für Mineralogie-Abhandlungen*, *172*, 381-408. https://doi.org/10.1127/njma/172/1998/381

Tomlinson, E. L., & Holland, T. J. (2021). A thermodynamic model for the subsolidus evolution and melting of peridotite. *Journal of Petrology*, *62*(1), egab012. https://doi.org/10.1093/petrology/egab045

Tomlinson, E. L., & Kamber, B. S. (2021). Depth-dependent peridotite-melt interaction and the origin of variable silica in the cratonic mantle. *Nature Communications*, *12*(1), 1082. https://doi.org/10.1038/s41467-021-21343-9

Tomlinson, E. L., Kamber, B. S., Hoare, B. C., Stead, C. V., & Ildefonse, B. (2018). An exsolution origin for Archean mantle garnet. *Geology*, *46*(2), 123-126. https://doi.org/10.1130/G39680.1

Vernon, R. (2011). Microstructures of melt-bearing regional metamorphic rocks. *Geological Society of America Memoirs*, *207*(1-11). https://doi.org/10.1130/2011.1207(01)

Vernon, R. H. (2018). *A practical guide to rock microstructure*. Cambridge university press. https://doi.org/10.1017/9781108654609

Walsh, C., Kamber, B. S., & Tomlinson, E. L. (2023). Deep, ultra-hot-melting residues as cradles of mantle diamond. *Nature*, *615*(7952), 450-454. https://doi.org/10.1038/s41586-022-05665-2

Walter, M. J. (1998). Melting of garnet peridotite and the origin of komatiite and depleted lithosphere. *Journal of Petrology*, *39*(1), 29-60. https://doi.org/10.1093/petroj/39.1.29

Wasch, L. J., van der Zwan, F. M., Nebel, O., Morel, M., Hellebrand, E. W., Pearson, D. G., & Davies, G. R. (2009). An alternative model for silica enrichment in the Kaapvaal subcontinental lithospheric mantle. *Geochimica et Cosmochimica Acta*, *73*(22), 6894-6917. https://doi.org/10.1016/j.gca.2009.07.038

Whitfield, G. (1973). The petrology and mineralogy of peridotite xenoliths from the Bultfontein, Wesselton, Dutoitspan and Roberts Victor kimberlites. International Kimberlite Conference: Extended Abstracts,

Whitney, D. L., & Evans, B. W. (2010). Abbreviations for names of rock-forming minerals. *American mineralogist*, *95*(1), 185. https://doi.org/10.2138/am.2010.3371

Wilson, A., & Bolhar, R. (2022). Olivine in komatiite records origin and travel from the deep upper mantle. *Geology*, *50*(3), 351-355. https://doi.org/10.1130/G49523.1

Wyman, D. (2018). Do cratons preserve evidence of stagnant lid tectonics? *Geoscience Frontiers*, *9*(1), 3-17. https://doi.org/10.1016/j.gsf.2017.02.001

Xu, H., Zhang, J., Yu, T., Rivers, M., Wang, Y., & Zhao, S. (2015). Crystallographic evidence for simultaneous growth in graphic granite. *Gondwana Research*, *27*(4), 1550-1559. https://doi.org/10.1016/j.gr.2014.01.013

Acknowledgments

This work was funded by Australian Research Council Discovery Project (DP220100136). We thank Emma Tomlinson and Carl Walsh for discussions and sharing thermodynamic model outputs and hand sample photographs. Joyjit Dey and Richard Walshaw collected the EBSD data. Ming Li and Sean Murray assisted with SEM-BSE imaging. We would also like to thank xxx and xxx for their constructive reviews, and xxx for editorial handling.

Author information

Authors and Affiliations

School of Natural Sciences, Macquarie University, Sydney, NSW 2109, Australia

Nathan R. Daczko & Robyn L. Gardner

School of Earth and Atmospheric Sciences, Queensland University of Technology, Brisbane, QLD 4000, Australia

Balz S. Kamber & Henrietta E. Cathey

School of Earth and Environment, University of Leeds, Leeds, UK

Sandra Piazolo

Corresponding author

Correspondence to Nathan R. Daczko.

Ethics declarations

Conflict of interest

The authors declare that this work does not bear any conflict of interest.

Figure and Table captions

Figure 1. Comparison of natural cratonic garnet-free peridotites (compilation of Tomlinson & Kamber, 2021) with melt depleted residues (i.e., the composition of solids after melt extraction) from experiments Walter (1998) and thermodynamic models (Tomlinson & Kamber, 2021; Walsh et al., 2023). (a) Garnet-free peridotites & experimental residues plotted on the IUGS ultramafic rock classification after Le Bas and Streckeisen (1991), excluding the pyroxenite fields (i.e., base of diagram is olivine = 40 vol%). The studied samples (bulk rock reconstituted from mineral modes and compositions; green symbols; number is last digit of sample identifiers) are shown in the context of other natural garnet-free peridotites from multiple cratons (Tomlinson & Kamber, 2021), with the Kaapvaal craton highlighted. (b) The same data as in (a) in a plot of olivine (Ol) modal abundance versus forsterite (Fo) content. At the dominant olivine composition of the Kaapvaal peridotites ($Fo_{92.5–93.5}$, horizontal band), the matching experimental residue is dunite. However, the Kaapvaal peridotites (including our samples) have lower modes of olivine, with excess orthopyroxene (Opx, >30% and up to 45–55%) and minor clinopyroxene (Cpx). (c) The same data as in (a) & (b) is used in a plot of SiO_2 vs MgO/SiO_2 with residues from the experiments of Walter (1998) divided

into 3GPa and > 3 GPa groups and the numerical models of Tomlinson and Kamber (2021) and Walsh et al. (2023). Selected high-temperature olivine and orthopyroxene compositions from the numerical models are plotted for reference (see discussion for details). Mineral abbreviations follow Whitney and Evans (2010).

Figure 2. Hand sample, photomicrograph and back-scattered electron (BSE) images of two representative spinel-facies harzburgite xenoliths, highlighting variable Opx colour and textural types of Cpx. This study finds that reactive flow of komatiite melt (melt_{in}) through precursor harzburgite increased the mode of Opx to form the SiO_2-enriched peridotite (Ol_1 + Opx_1 + minor Cpx_1) xenoliths examined (see reactions R1 and R2 on Fig. 9). (a) Sample 17BSK041 with brown and reflective ('bronzitic') Opx. (b) Sample 17BSK045 with green Opx. White arrows in hand sample images point to light reflection off Opx cleavage planes, enhanced in more 'bronzitic' samples. Three microstructural types of rare Cpx are distinguished: (i) Cpx_1 forms films and occurs with or without fine-grained Ol_1 (BSE and cross polarised light (XPL) insets in (b)); (ii) Cpx_2 forms intergrowths with spinel (Cpx_2-Spl_1 in (a)); (iii) Cpx_3 (lacking exsolutions) occurs in spinel-lherzolite (Samples 17BSK039 and 040), associated with rare garnet (Grt); and (iv) Cpx_{lam} forms exsolution lamellae in Opx_1 (BSE inset in (a)).

Figure 3. Microstructures of representative harzburgite sample 17BSK046. (a) Phase map drawn from photomicrographs, highlighting apparent low dihedral angles (red arrows), mineral films (green stars), cuspate boundaries (grey arrows), irregular grain shapes, undulating grain boundaries (example labelled), apparent inclusions (example labelled) and clusters of nearby minerals with similar crystal orientation, (numbered 1 to 5 in (b) and (c)); white solid boxes highlight areas shown in (b)–(f) and location of Figure 5. (b) and (c) show EBSD maps with band contrast background showing interconnection of minerals with Ol and Opx, respectively, Z-axis orientations coloured using the inverse pole figure (IPF) scheme; rare subgrain (<5°) boundaries are white. Note: late serpentinization is the darkest grey areas in the band contrast image. Insets show pole figures of examples of neighbourhoods of grains (marked 1 to 5) with the same orientation suggesting these are single crystals connected in 3D; blue and orange arrows show location of cumulative misorientation profiles across selected grains (graph insets) which highlight orientation change and subgrain boundaries (tick marks

on arrows). (d)–(f) XPL photomicrographs of microstructures, with some grain boundaries highlighted by white dashed lines; key features include mineral films, low dihedral angles (tip highlighted by red line), 120° angle triple junctions and clusters of nearby minerals with similar extinction angles in 2D, assumed to be connected in 3D. Note: deformation twins are not observed.

Figure 4. Dominant slip system analysis of 2–5° subgrain boundaries. (a) Boundary inverse pole figures (IPF) in crystal symmetry for Ol (fabric intensity indicated by multiple of uniform density (MUD) = 0–6 and Opx MUD = 0–7) in the harzburgite and lherzolite samples; dominant slip system(s) specified with type, plane and direction of slip identified, n is the number of points in the boundary analysis for the sample. (b) Guide for determining Ol common slip systems after Ruzicka and Hugo (2018) and Griffin et al. (2022); Ol crystal cartoon shows the dominant Type B slip system (010)[001] measured in samples 17BSK041 to 048, which has rotation on the a-axis, slip on the b plane in the c direction. (c) Guide for determining Opx common slip systems after Bernard et al. (2021); Opx crystal cartoon shows the Type BA slip system (010)[100], which has rotation on the c-axis, slip on the b plane in the a direction. Note***: Sample 17BSK044 Opx MUD range is from 0 to 33.55 rather than the standard range 0-7 used for enstatite in the other samples. The higher MUD is an artefact of coarser Cpx_3 exsolution lamellae in Opx.

Figure 5. Representative Cpx_2-Spl_1 vermicular symplectite (sample 17BSK046). EBSD maps with band contrast backgrounds of (a) phases and (b) Z-axis orientations coloured using the IPF scheme. The colour IPF distribution shows that Cpx and Spl each have a single orientation. (c) Pole figures for Opx, Cpx and Spl showing all points for the map with colours corresponding to the IPF map in (b). One of the Spl {110} orientations replicates both Cpx and Opx {010}, highlighted by black dashed circles. In addition, one Spl {111} orientation replicates Cpx and Opx {100}, highlighted by red dashed circles. This study finds that reactive flow of komatiite melt ($melt_{in}$) formed these symplectites which epitaxially replace earlier Opx_1 (see reaction R3 on Fig. 9). Additionally, the grain boundary relationships indicate that the symplectites likely also replace some Ol_1 (see reaction R4 on Fig. 9).

Figure 6. Microstructures of representative lherzolite sample 17BSK039. (a)) Phase map drawn from photomicrographs, highlighting apparent low dihedral angles (red arrows), mineral films (green stars), cuspate fingers (grey arrows), irregular grain shapes, undulating grain boundaries (example labelled), apparent inclusions (example labelled) and clusters of nearby minerals with similar crystal orientation, (numbered 1 to 4 in (b) and (c)); white solid boxes highlight areas shown in (b)–(f) and location of Figure 7a; (b) and (c) show EBSD maps with band contrast background showing interconnection of minerals with Ol and Opx, respectively, Z-axis orientations coloured using the IPF scheme; rare subgrain (<5°) boundaries are white. Note: late serpentinization is the darkest grey areas in the band contrast image. Insets show pole figures of examples of neighbourhoods of grains (marked 1 to 4) with the same orientation suggesting these are single crystals connected in 3D; (d)–(e) XPL photomicrographs and (f) BSE image showing mineral films (Opx_1, Cpx_1, Grt_1), low dihedral angles, 120° angle triple junctions and clusters of nearby minerals with similar extinction angles in 2D, assumed to be connected in 3D. This study finds that reactive flow of komatiite melt likely involved late crystallisation of Grt_1 in grain boundary films and cross-cutting textures (see reaction R5 on Fig. 9). Note: Cpx_{lam} are enhanced near Grt_1 (f) and deformation twins are not observed.

Figure 7. Cpx_3-Grt_2-Spl_2-Ol_2 symplectite in sample 17BSK039. (a) Line drawing photomicrographs showing location of the symplectite and minor late amphibole (Amp). (b) EBSD phase map of the symplectite showing intergrowth of Cpx_3, Grt_2, Spl_2 and Ol_2. (c) Z-axis orientations coloured using the IPF scheme, where matching colours between the grains indicate similar orientations. (d) XPL photomicrograph of new Ol_2 in the symplectite. (e) Pole figures showing similar orientation for (i) partially replaced Ol_1 grain A {010} with Spl_2 {110} (purple circles and dashed line); (ii) partially replaced Ol_1 grain A {001} with Spl_2 {111} (red circles and dashed line); (iii) Opx_1 grain C {100} with Cpx_1 grains G and H {100} and Grt_2 {110} (green circles and dashed line); (iv) Opx_1 grain C {010} with Cpx_1 grains G and H {010}, and Grt_2 and Spl_2 {100} (black circles and dashed line); (v) Opx_1 grain C {001} with Grt_2 {110} and Spl_2 {100} (blue circles and dashed line). Only a subset of the mineral grains with orientations replicating Ol_1 grain A and Opx_1 grain C have been included to simplify the analysis. The full pole figures with

orientations replicating Opx_1 grains D and E are available in Online resource 2 - Supplementary Figure 3. This study finds that reactive flow of komatiite melt likely formed these symplectites which epitaxially replace earlier Opx_1 and Ol_1 (see reaction R6 on Fig. 9).

Figure 8. Impact of fine lamellae on pyroxene mineral chemistry analysis. (a) Analysis locations in 17BSK039 were chosen in inclusion-free areas (white symbols) and where the beam overlapped lamellae evident in BSE (coloured symbols). Spl analyses from symplectites are also plotted for comparison. (b) and (c) BSE images of Cpx lamellae (Cpx_{lam}) in Opx_1 in harzburgite (b; 17BSK045) and lherzolite (c; 17BSK039). (d) Opx lamellae (Opx_{lam}) in Cpx_1 in lherzolite (17BSK039). Note: similar lamellae are seen in Cpx_2 but not in Cpx_3.

Figure 9: Modelled mode changes of phases during assimilation and crystallisation following hybridisation of komatiite with peridotite as a function of temperature, using the data from (a) Tomlinson and Kamber (2021) and (b) Walsh et al. (2023). Increased and decreased modes are relative to the modes in the original system state (1:1 solid:liquid in panel (a) and 2:1 solid:liquid in panel (b)). Increased modes indicate enrichment of the phase by crystallisation, whereas decreased modes indicate total or partial consumption of the phase by assimilation. A negative slope indicates increasing modes, whereas a positive slope indicates consumption of the phase in reactions (i.e., Ol is consumed in temperature range 6, and Opx is consumed in temperature ranges 3–6 and 9–10). See Table 2 for a summary of komatiite and hybrid system compositions. Black text: stable minerals, both in excess (noted with a subscript) or only partially consumed (i.e. decreased modes) relative to the original system state. Black italics: minerals partially consumed upon cooling, but still in excess. Purple text: melt-rock reactions inferred from microstructural observations. Purple italics: cooling exsolution lamellae developed at temperatures not modelled. (c) and (d) Chemical bivariant plots showing mixing (dashed line with 20% increments) between high temperature Opx compositions (#1, #2 extracted from the temperature ranges in (a) and (b), respectively) and precursor peridotites (pink squares, used in the models in (a) and (b)). Other data is from the same sources as Fig. 1. See Table 2 for a summary of compositions.

Table 1. Sample mineralogy, modes, and olivine Fo content, ordered by orthopyroxene mode.

Sample ID	Group	EBSD mode (vol%) *[italics = SEM-EDX mode]*						EMPA Olivine Fo content %	stdev
		ol	opx	cpx	grt	spn	phl		
17BSK041	Group 1 harzburgite	62.58	33.12	2.58	–	0.11	1.61	93.02[$]	0.04
17BSK048		60.20	37.27	1.87	–	0.66	–	93.16	0.06
17BSK046		55.53	43.37	0.88	–	0.22	–	92.99	0.07
17BSK045[&]		49.05	50.95	0.37	–	0.03	–	92.98	0.08
17BSK043[#]		43.63	54.90	1.10	–	0.37	–	93.05	0.09
17BSK039	Group 2 lherzolite	62.78	30.04	5.38	1.23	0.56	–	92.91	0.11
17BSK040		*49.46*	*44.41*	*5.62*	*0.20*	*0.30*	–	92.56	0.04
17BSK044		47.62	44.71	7.56	–	0.11	–	92.27	0.06

[$] olivine mineral chemistry from SEM-EDX analyses conducted by Kamber and Tomlinson (2019)

[&] cpx and spn not indexed EBSD, semi-quantitative estimates by image analysis in reflected and cross-polarised light

[#] modal abundance determined by pixel classification of blended optical thin section scans with method of Acevedo Zamora and Kamber (2023)

Table 2. Bulk rock compositions for the studied samples (reconstituted from mineral modes and compositions), and bulk rock mixing calculations. Data sources: Tomlinson

and Kamber (2021), Walsh et al. (2023), Condie (1993), Heilimo et al. (2010) and DIGIS Team (2021).

Samples	Densities					SiO$_2$	TiO$_2$	Al$_2$O$_3$	Cr$_2$O$_3$	FeO	NiO	MnO	MgO	CaO	Na$_2$O	K$_2$O	TOTAL	MgO/SiO$_2$	Mg#
Reconstituted bulk rock compositions																			
	Ol	Opx	Cpx	Grt	Spn														
17BSK048	3.30	3.25	3.25		4.59	46.77	0.00	1.15	0.81	5.76	0.25	0.10	44.36	0.77	0.02	0.00	100.0	0.95	93.2
17BSK046	3.31	3.25	3.25		4.55	47.91	0.00	1.21	0.53	5.71	0.25	0.10	43.73	0.54	0.02	0.00	100.0	0.91	93.2
17BSK045	3.31	3.25	3.25		4.56	48.97	0.00	1.16	0.40	5.57	0.24	0.10	43.00	0.54	0.02	0.00	100.0	0.88	93.2
17BSK043	3.30	3.25	3.25		4.51	49.32	0.00	1.68	0.71	5.38	0.21	0.10	41.82	0.75	0.03	0.00	100.0	0.85	93.3
17BSK039	3.31	3.25	3.25	3.71	4.50	45.78	0.00	1.63	0.57	6.18	0.28	0.10	43.86	1.54	0.06	0.00	100.0	0.96	92.7
17BSK040	3.31	3.25	3.25	3.72	4.51	48.58	0.00	1.32	0.42	5.91	0.27	0.10	41.71	1.61	0.08	0.00	100.0	0.86	92.6
17BSK044	3.31	3.25	3.25		4.64	48.72	0.00	0.73	0.87	6.12	0.19	0.11	41.22	1.93	0.10	0.00	100.0	0.85	92.3
					Average SiO$_2$ in 045 and 043	*49.1*													
Two precursor harzburgite compositons [pink squares, Fig. 9c,d], their average and two komatiite compositions used in the thermodynamic models																			
Harzburgite residue (Ol:Opx 75:25) after lherzolite (KR4003) melting at 1500°C and 2GPa$^{\#}$						44.38	0.01	1.30	0.43	6.94	0.00	0.00	46.46	0.46	0.01	0.00	100.0	1.05	92.3
Harzburgite residue (Ol:Opx 88:12) after lherzolite (KR4003) melting at 1630°C and 3GPa$^{\#}$						43.14	0.00	0.54	0.22	6.08	0.00	0.00	49.84	0.18	0.01	0.00	100.0	1.16	93.6
Komatiite$^{\#}$, run 78, 8 GPa, 1900°C, Takahashi (1986)						46.60	0.20	4.60	0.40	8.80	–	0.20	34.90	3.90	0.30	–	99.9	0.75	87.6
Komatiite$^{\&}$, run 70.08, 7 GPa, 1850 °C, Walter (1998)						47.33	0.28	6.45	0.50	8.61	–	0.18	30.29	5.61	0.41	0.11	99.8	0.64	86.2
1:1 lherzolite:komatiite, 2 GPa, Tomlinson & Kamber (2021)						45.75	0.18	4.43	0.41	8.41	–	–	36.10	3.68	0.26	0.05	99.36	0.79	89.8
2:1 harzburgite:komatiite, 3 GPa, Walsh et al. (2023)						45.66	0.13	4.32	0.48	7.11	–	–	39.54	2.40	0.19	0.04	99.87	0.87	91.6
Average 'refractory harzburgite' (used below) = average of two harzburgite residues						*43.8*	*0.01*	*0.92*	*0.33*	*6.51*	*0.00*	*0.00*	*48.15*	*0.32*	*0.01*	*0.00*	*100.0*	*1.10*	*92.9*
Infiltrating highly Si-rich liquids hybridised with average mantle, see Discussion																			
Hypothetical pure SiO$_2$ liquid						100.00	0.00	0.00	0.00	0.00		0.00	0.00	0.00	0.00	0.00	100.0		
Avg. Archean TTG$^{\$}$						70.03	0.34	15.22	0.00	3.53		0.00	1.11	2.82	4.53	2.42	100.0	0.02	35.9
Avg. Karelian sanukitoid*						65.58	0.51	15.93	0.00	4.23		0.08	2.66	3.63	4.52	2.86	100.0	0.04	52.8
Avg. modern boninite^						58.25	0.25	13.34	0.03	8.23		0.14	9.10	8.21	1.99	0.47	100.0	0.16	66.4
Calculated hybridised compositions					**Melt %**														
Avg. 'refractory harzburgite' + hypothetical pure SiO$_2$ liquid					9.6	*49.1*	0.01	0.83	0.29	5.89	0.00	0.00	43.54	0.29	0.01	0.00	100.0	0.89	93.1
Avg. 'refractory harzburgite' + avg. Archean TTG					20.5	*49.1*	0.07	3.85	0.26	5.90	0.00	0.00	38.51	0.84	0.94	0.50	100.0	0.78	92.2
Avg. 'refractory harzburgite' + avg. Karelian sanukitoid					24.7	*49.1*	0.13	4.62	0.24	5.95	0.00	0.02	36.92	1.14	1.12	0.71	100.0	0.75	91.8

Avg. 'refractory harzburgite' + avg. modern boninite		37.2	*49.1*	0.10	5.53	0.21	7.15	0.00	0.05	33.64	3.25	0.74	0.18	100.0	0.68	89.4
Modelled 'reactive flow': extraction of high-temperature liquids leaving Ol+Opx residues averaged over the temperature ranges #1 (Fig. 9a) and #2 (Fig. 9b)																
	P (GPa)	T and liquid fraction; T range and modes														
Evolved liquid #1[#]	2	1553°C, 44% liquid remaining	49.09	0.41	9.42	0.52	10.39	0.00	0.00	21.04	8.29	0.60	0.22	100.0	0.43	81.9
Ol+Opx solid #1[#]		1553–1500°C (92% opx + 8% ol)	51.29	0.09	5.98	0.98	10.28	0.00	0.00	28.00	3.19	0.15	0.03	100.0	0.55	82.9
Evolved liquid #2[&]	3	1681°C, 57% liquid remaining	48.92	0.24	7.90	0.94	9.11	0.00	0.00	28.10	4.35	0.36	0.07	100.0	0.57	84.6
Ol+Opx solid #2[&]		1681–1630°C (85% opx + 15% ol)	51.44	0.01	4.70	1.60	7.13	0.00	0.00	34.59	0.49	0.04	0.00	100.0	0.67	89.6
Calculated Opx-enriched peridotite		**Added Ol+Opx solid %**														
2 GPa harzburgite residue + Opx-Ol solid #1		50	47.84	0.05	3.64	0.70	8.61			37.23	1.83	0.08	0.02	100.0	0.78	88.5
3 GPa harzburgite residue + Opx-Ol solid #2		50	47.29	0.01	2.62	0.91	6.60			42.21	0.34	0.02	0.00	100.0	0.89	91.9

Online Resources

The following Online Resources are provided:

Online Resource 1 (ESM_1.pdf: Supplementary Methods)

Online Resource 2 (ESM_2.pdf: Supplementary Figures 1–4)

Online Resource 3 (ESM_3.xlsx sheet a and h: Details of electron microprobe analyses method and CRMs, respectively)

Online Resource 3 (ESM_3.xlsx sheet b-g: Individual olivine, orthopyroxene, clinopyroxene, spinel, garnet and amphibole electron microprobe analyses, respectively)

Online Resource 4 (ESM_4.xlsx: summaries of mineral electron microprobe analyses)

Online Resource 5 (ESM_5.xlsx: Table 2 with bivariate plots of bulk geochemical data

Online Resource 6 (ESM_6.xlsx: 3 GPa outputs from thermodynamic model of Walsh et al. (2023))

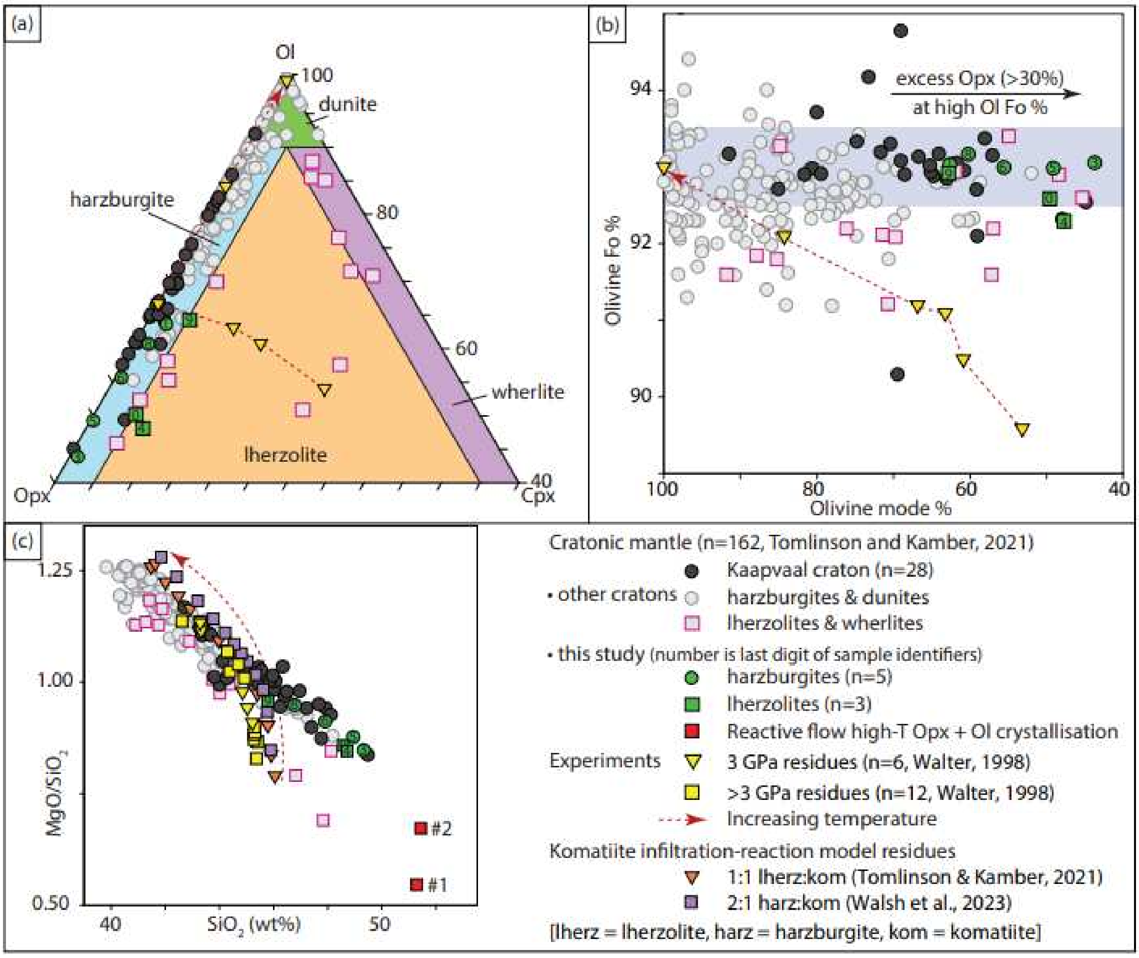
(a)
Ol
100
dunite
harzburgite
80
60
wherlite
lherzolite
Opx
40
Cpx
(b)
94
92
90
Olivine Fo %
excess Opx (>30%)
at high Ol Fo %
100
80
60
40
Olivine mode %
(c)
1.25
1.00
0.50
MgO/SiO$_2$
40
SiO$_2$ (wt%)
50
#2
#1
Cratonic mantle (n=162, Tomlinson and Kamber, 2021)
Kaapvaal craton (n=28)
• other cratons
harzburgites & dunites
lherzolites & wherlites
• this study (number is last digit of sample identifiers)
harzburgites (n=5)
lherzolites (n=3)
Reactive flow high-T Opx + Ol crystallisation
Experiments
3 GPa residues (n=6, Walter, 1998)
>3 GPa residues (n=12, Walter, 1998)
Increasing temperature
Komatiite infiltration-reaction model residues
1:1 lherz:kom (Tomlinson & Kamber, 2021)
2:1 harz:kom (Walsh et al., 2023)
[lherz = lherzolite, harz = harzburgite, kom = komatiite]

Figure 1

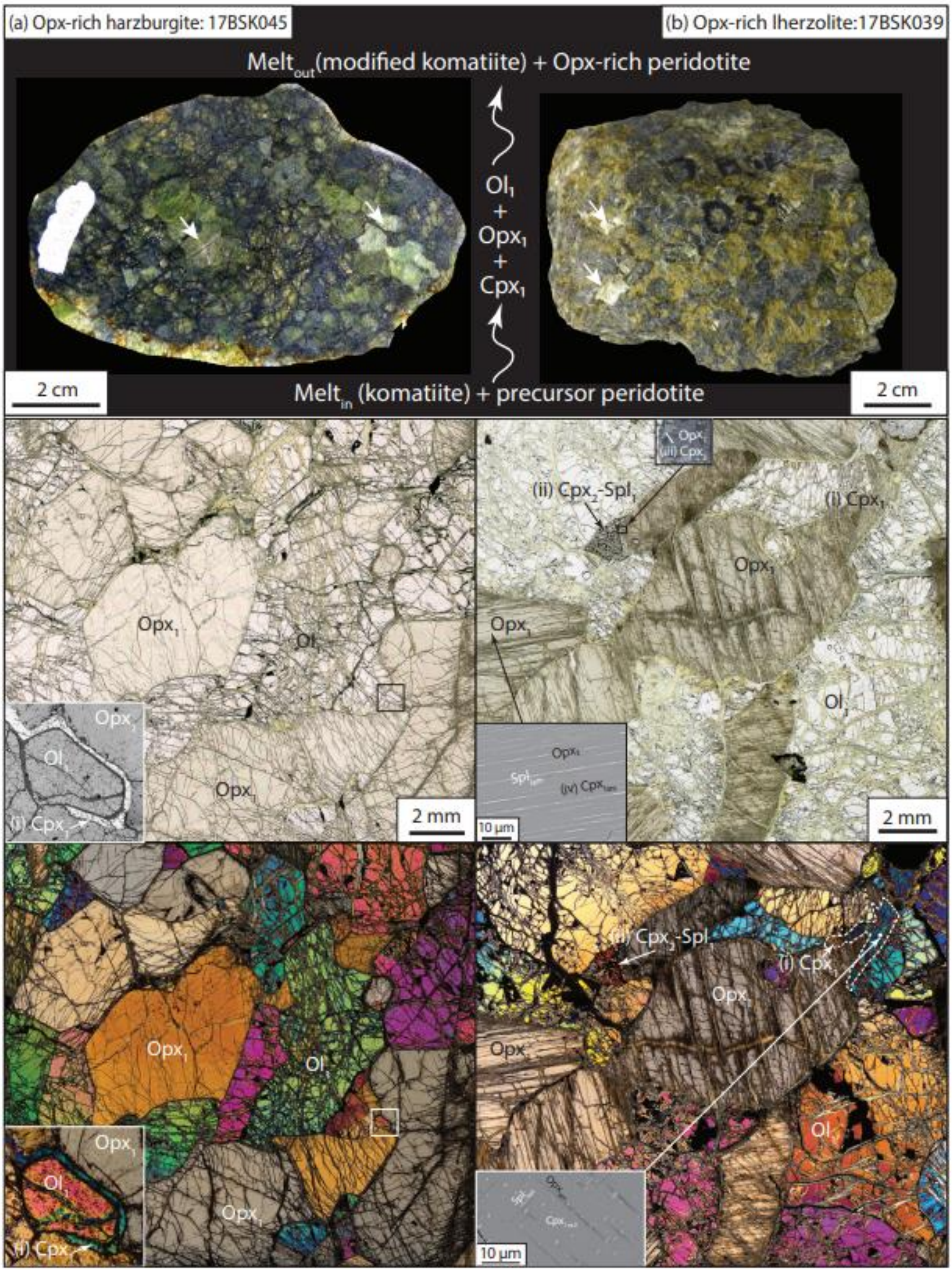
(a) Opx-rich harzburgite: 17BSK045
(b) Opx-rich lherzolite:17BSK039
Melt$_{out}$(modified komatiite) + Opx-rich peridotite
Ol$_1$
+
Opx$_1$
+
Cpx$_1$
Melt$_{in}$ (komatiite) + precursor peridotite
2 cm
2 cm
Opx$_1$
Ol$_1$
Opx$_1$
Opx$_1$
Ol$_1$
(i) Cpx$_1$
2 mm
(ii) Cpx$_2$-Spl$_1$
(i) Cpx$_1$
Opx$_1$
(iii) Cpx$_2$
Opx$_1$
Ol$_1$
Opx$_1$
Spl$_{lam}$
(iv) Cpx$_{lam}$
10 µm
2 mm
Opx$_1$
Ol$_1$
Opx$_1$
Opx$_1$
Ol$_1$
(i) Cpx$_1$
(ii) Cpx$_2$-Spl$_1$
(i) Cpx$_1$
Opx$_1$
Opx$_1$
Ol$_1$
Spl$_{lam}$
Opx$_{lam}$
Cpx$_{lam}$
10 µm

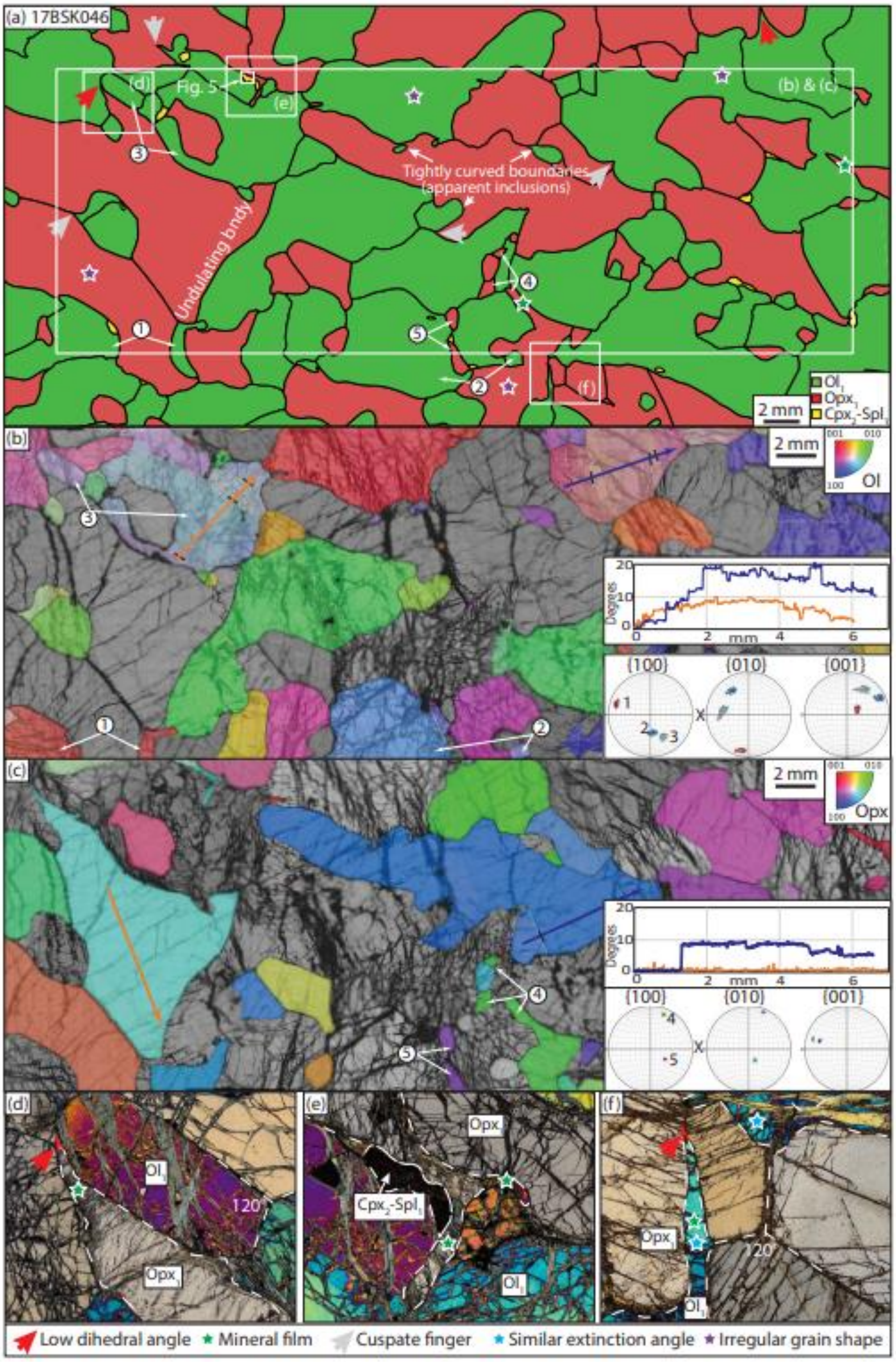
(a) 17BSK046
(d)
Fig. 5
(e)
(b) & (c)
③
Tightly curved boundaries (apparent inclusions)
Undulating bndy
④
⑤
①
②
(f)
Ol_1
Opx_1
Cpx_2-Spl_1
2 mm
(b)
2 mm
001 010 100 Ol
③
Degrees
0 10 20
0 2 mm 4 6
{100} {010} {001}
1 2 3
X
①
②
(c)
2 mm
001 010 100 Opx
Degrees
0 10 20
0 2 mm 4 6
{100} {010} {001}
4 5
X
④
⑤
(d)
Ol_1
120
Opx_1
(e)
Opx_1
Cpx_2-Spl_1
Ol_1
(f)
Opx_1
120
Ol_1
Low dihedral angle
Mineral film
Cuspate finger
Similar extinction angle
Irregular grain shape

Figure 3

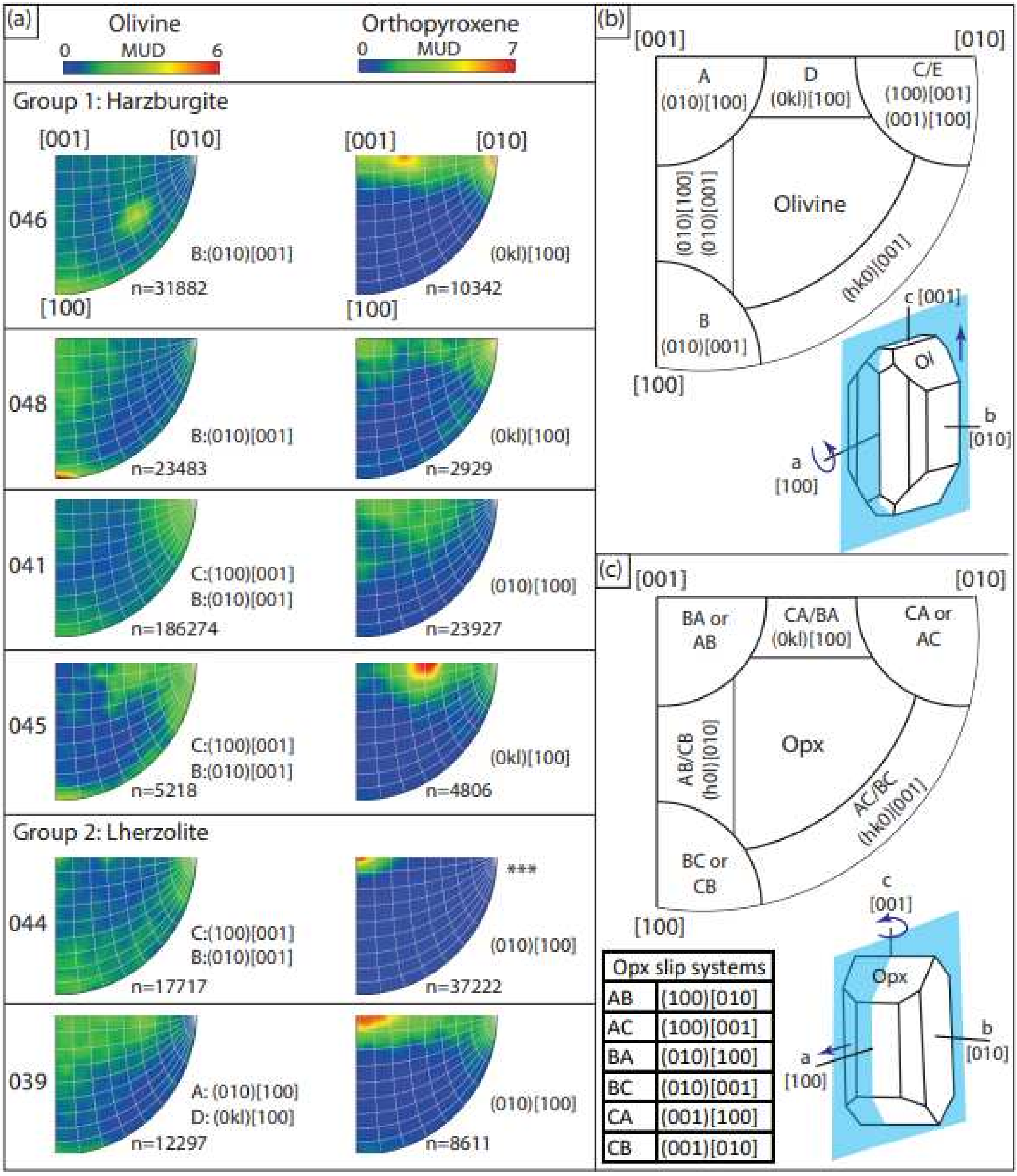

Opx slip systems	
AB	(100)[010]
AC	(100)[001]
BA	(010)[100]
BC	(010)[001]
CA	(001)[100]
CB	(001)[010]

Figure 4

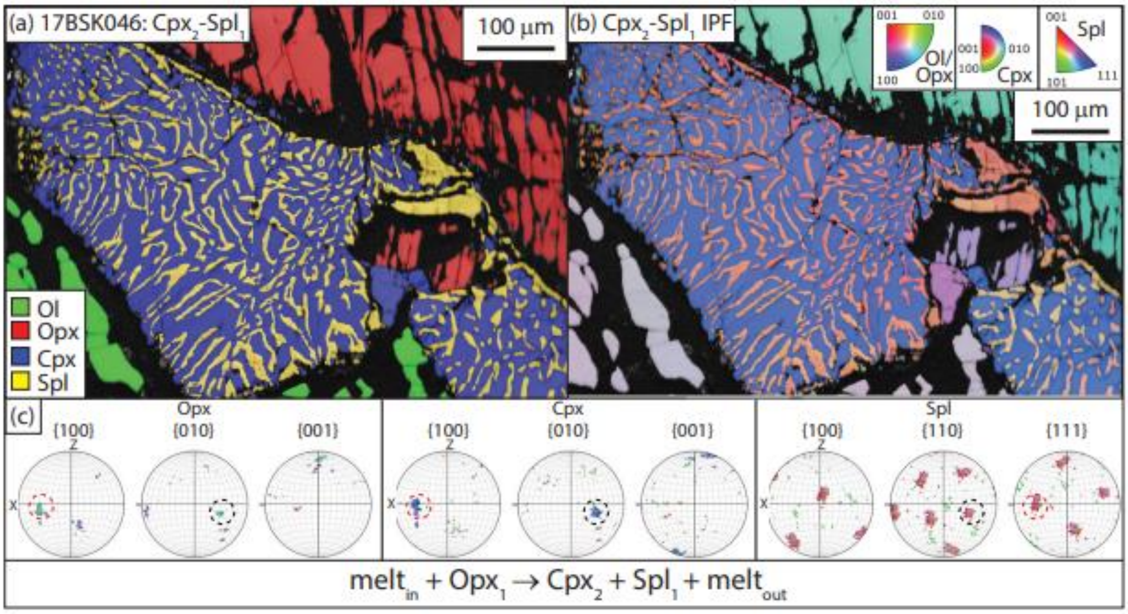
(a) 17BSK046: Cpx_2-Spl_1
100 μm
Ol
Opx
Cpx
Spl
(b) Cpx_2-Spl_1 IPF
001
010
100
Ol/Opx
Cpx
Spl
101
111
100 μm
(c)
Opx
{100}
{010}
{001}
Cpx
{100}
{010}
{001}
Spl
{100}
{110}
{111}
Z
X
$melt_{in} + Opx_1 \rightarrow Cpx_2 + Spl_1 + melt_{out}$

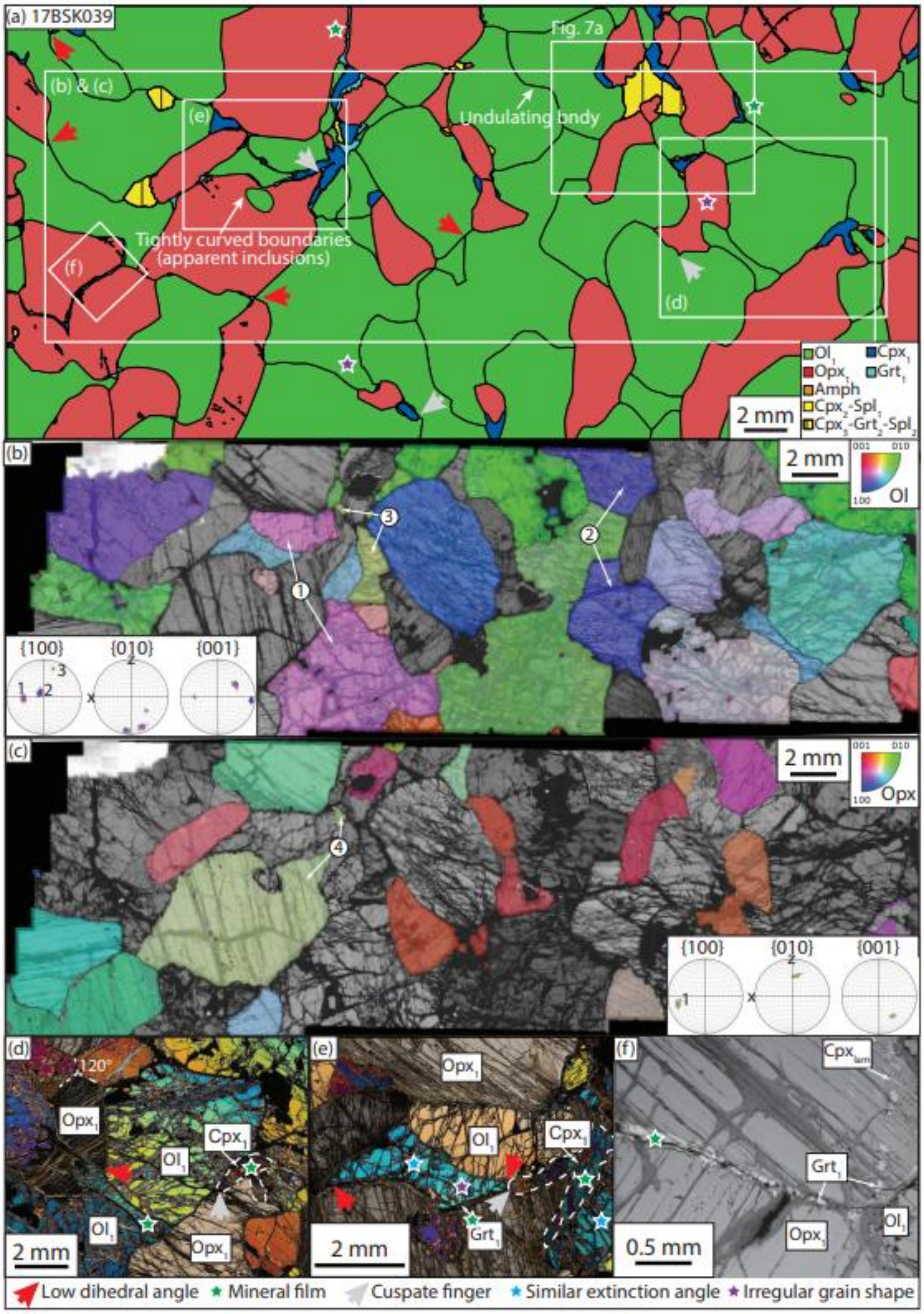
(a) 17BSK039
Fig. 7a
(b) & (c)
(e)
Undulating bndy
Tightly curved boundaries (apparent inclusions)
(f)
(d)
🟩Ol$_1$
🟥Opx$_1$
Amph
Cpx$_2$-Spl$_1$
Cpx$_3$-Grt$_2$-Spl$_2$
Cpx$_1$
Grt$_1$
2 mm
(b)
2 mm
001 010 100 Ol
{100} {010} {001}
1 2 3
z
x
①
②
③
(c)
2 mm
001 010 100 Opx
④
{100} {010} {001}
1
(d)
120°
Opx$_1$
Ol$_1$
Cpx$_1$
Ol$_1$
Opx$_1$
2 mm
(e)
Opx$_1$
Ol$_1$
Cpx$_1$
Grt$_1$
2 mm
(f)
Cpx$_{lam}$
Grt$_1$
Opx$_1$
Ol$_1$
0.5 mm
Low dihedral angle
Mineral film
Cuspate finger
Similar extinction angle
Irregular grain shape

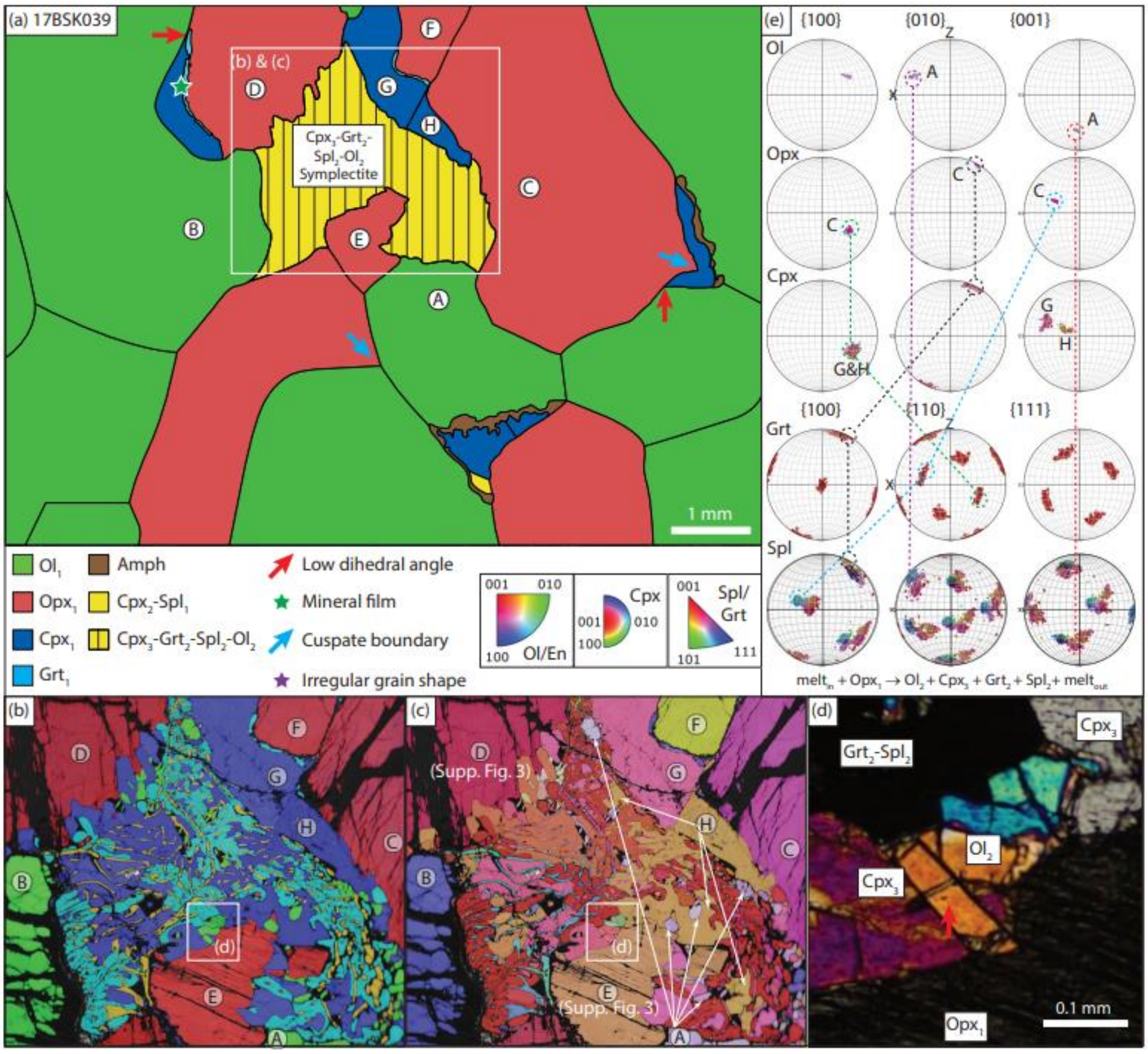

(a) 17BSK039
(b) & (c)
Cpx$_3$-Grt$_2$-Spl$_2$-Ol$_2$ Symplectite
A
B
C
D
E
F
G
H
1 mm
Ol$_1$
Opx$_1$
Cpx$_1$
Grt$_1$
Amph
Cpx$_2$-Spl$_1$
Cpx$_3$-Grt$_2$-Spl$_2$-Ol$_2$
Low dihedral angle
Mineral film
Cuspate boundary
Irregular grain shape
001
010
100
Ol/En
Cpx
001
010
100
Spl/Grt
001
101
111
(e)
{100}
{010}
{001}
Z
X
Ol
Opx
Cpx
Grt
Spl
{100}
{110}
{111}
G&H
melt$_{in}$ + Opx$_1$ → Ol$_2$ + Cpx$_3$ + Grt$_2$ + Spl$_2$ + melt$_{out}$
(b)
(c)
(Supp. Fig. 3)
(d)
Grt$_2$-Spl$_2$
Cpx$_3$
Ol$_2$
Opx$_1$
0.1 mm

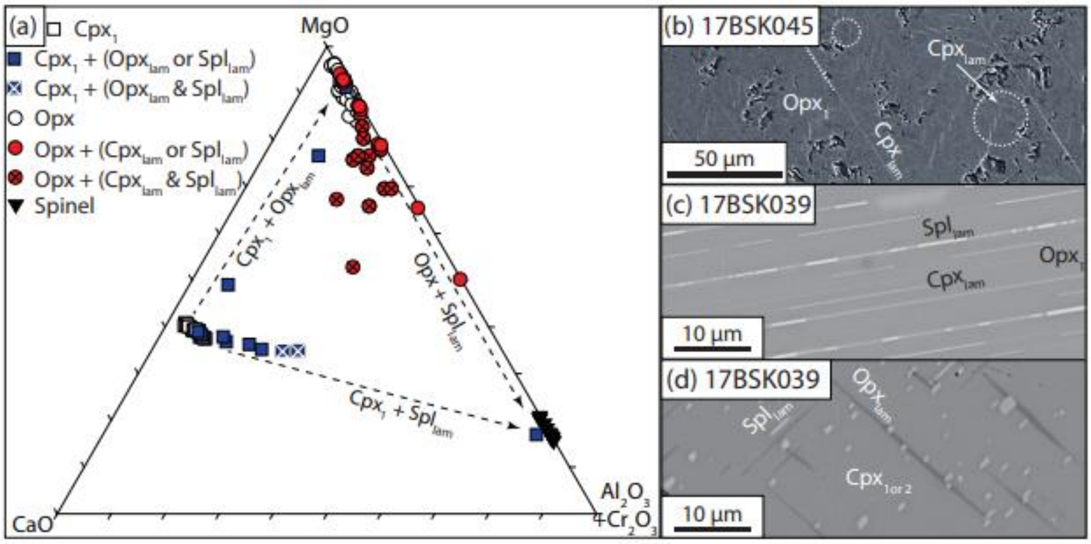
(a)
Cpx$_1$
Cpx$_1$ + (Opx$_{lam}$ or Spl$_{lam}$)
Cpx$_1$ + (Opx$_{lam}$ & Spl$_{lam}$)
Opx
Opx + (Cpx$_{lam}$ or Spl$_{lam}$)
Opx + (Cpx$_{lam}$ & Spl$_{lam}$)
Spinel
MgO
CaO
Al$_2$O$_3$ +Cr$_2$O$_3$
Cpx$_1$ + Opx$_{lam}$
Opx + Spl$_{lam}$
Cpx$_1$ + Spl$_{lam}$
(b) 17BSK045
Cpx$_{lam}$
Opx$_1$
Cpx$_{lam}$
50 µm
(c) 17BSK039
Spl$_{lam}$
Opx$_1$
Cpx$_{lam}$
10 µm
(d) 17BSK039
Opx$_{lam}$
Spl$_{lam}$
Cpx$_{1 or 2}$
10 µm

Figure 8

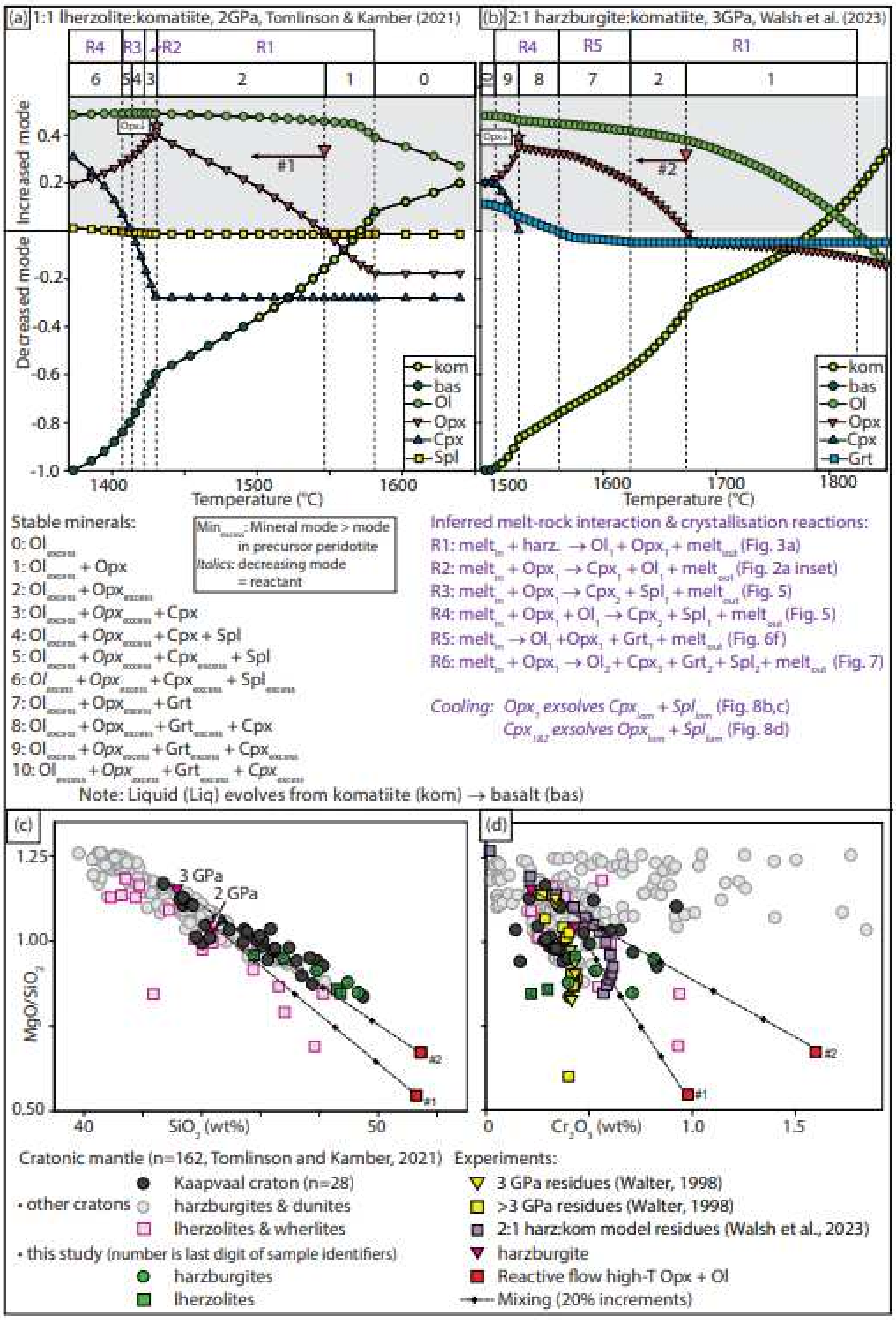
(a) 1:1 lherzolite:komatiite, 2GPa, Tomlinson & Kamber (2021)
R4 R3 R2 R1
6 5 4 3 2 1 0
Opx1
#1
Increased mode
Decreased mode
0.4
0.2
-0.2
-0.4
-0.6
-0.8
-1.0
1400
1500
1600
Temperature (°C)
kom
bas
Ol
Opx
Cpx
Spl
(b) 2:1 harzburgite:komatiite, 3GPa, Walsh et al. (2023)
R4 R5 R1
10 9 8 7 2 1
Opx1
#2
1500
1600
1700
1800
Temperature (°C)
kom
bas
Ol
Opx
Cpx
Grt
Stable minerals:
0: Ol_{excess}
1: Ol_{excess} + Opx
2: Ol_{excess} + Opx_{excess}
3: Ol_{excess} + Opx_{excess} + Cpx
4: Ol_{excess} + Opx_{excess} + Cpx + Spl
5: Ol_{excess} + Opx_{excess} + Cpx_{excess} + Spl
6: Ol_{excess} + Opx_{excess} + Cpx_{excess} + Spl_{excess}
7: Ol_{excess} + Opx_{excess} + Grt
8: Ol_{excess} + Opx_{excess} + Grt_{excess} + Cpx
9: Ol_{excess} + Opx_{excess} + Grt_{excess} + Cpx_{excess}
10: Ol_{excess} + Opx_{excess} + Grt_{excess} + Cpx_{excess}
Min_{excess}: Mineral mode > mode in precursor peridotite
Italics: decreasing mode = reactant
Inferred melt-rock interaction & crystallisation reactions:
R1: $melt_{in}$ + harz. → Ol_1 + Opx_1 + $melt_{out}$ (Fig. 3a)
R2: $melt_{in}$ + Opx_1 → Cpx_1 + Ol_1 + $melt_{out}$ (Fig. 2a inset)
R3: $melt_{in}$ + Opx_1 → Cpx_2 + Spl_1 + $melt_{out}$ (Fig. 5)
R4: $melt_{in}$ + Opx_1 + Ol_1 → Cpx_2 + Spl_1 + $melt_{out}$ (Fig. 5)
R5: $melt_{in}$ → Ol_1 + Opx_1 + Grt_1 + $melt_{out}$ (Fig. 6f)
R6: $melt_{in}$ + Opx_1 → Ol_2 + Cpx_3 + Grt_2 + Spl_2 + $melt_{out}$ (Fig. 7)
Cooling: Opx_1 exsolves Cpx_{lam} + Spl_{lam} (Fig. 8b,c)
$Cpx_{1\&2}$ exsolves Opx_{lam} + Spl_{lam} (Fig. 8d)
Note: Liquid (Liq) evolves from komatiite (kom) → basalt (bas)
(c)
1.25
1.00
0.50
MgO/SiO_2
3 GPa
2 GPa
#2
#1
40
50
SiO_2 (wt%)
(d)
0
1.0
1.5
Cr_2O_3 (wt%)
#2
#1
Cratonic mantle (n=162, Tomlinson and Kamber, 2021)
● Kaapvaal craton (n=28)
• other cratons ○ harzburgites & dunites
☐ lherzolites & wherlites
• this study (number is last digit of sample identifiers)
● harzburgites
■ lherzolites
Experiments:
▽ 3 GPa residues (Walter, 1998)
☐ >3 GPa residues (Walter, 1998)
■ 2:1 harz:kom model residues (Walsh et al., 2023)
▼ harzburgite
■ Reactive flow high-T Opx + Ol
Mixing (20% increments)

Figure 9